

## **General Disclaimer**

### **One or more of the Following Statements may affect this Document**

- This document has been reproduced from the best copy furnished by the organizational source. It is being released in the interest of making available as much information as possible.
- This document may contain data, which exceeds the sheet parameters. It was furnished in this condition by the organizational source and is the best copy available.
- This document may contain tone-on-tone or color graphs, charts and/or pictures, which have been reproduced in black and white.
- This document is paginated as submitted by the original source.
- Portions of this document are not fully legible due to the historical nature of some of the material. However, it is the best reproduction available from the original submission.

NASA Contractor Report 141438

## Analysis of Satellite-to-Satellite Tracking (SST) and Altimetry Data from GEOS-C

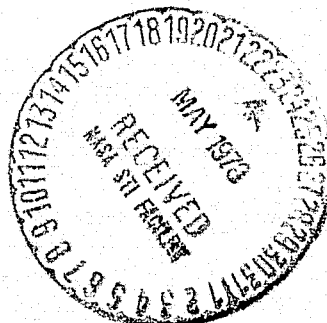
(NASA-CR-141438) ANALYSIS OF  
SATELLITE-TO-SATELLITE TRACKING (SST) AND  
ALTIMETRY DATA FROM GEOS-C (Aerospace Corp.,  
El Segundo, Calif.) 77 p HC A05/MF A01

N78-22133

Unclas  
CSCI 22A G3/13 16628

L. Wong  
E. Matthews  
and  
W. Downs

April 1978



National Aeronautics and  
Space Administration

**Wallops Flight Center**  
Wallops Island, Virginia 23337  
AC 804 824-3411

NASA Contractor Report 141438

## Analysis of Satellite-to-Satellite Tracking (SST) and Altimetry Data from GEOS-C

L. Wong  
E. Matthews  
and  
W. Downs

The Aerospace Corporation  
Development Operation  
EL Segundo, Ca. 90245

Prepared Under Contract No. NAS6-2508



National Aeronautics and  
Space Administration

**Wallops Flight Center**

Wallops Island, Virginia 23337  
AC 804 824-3411

#### ACKNOWLEDGEMENT

The authors wish to thank Mr. J. Marsh and R. Stanley of NASA; Dr. J. Wertz, Messrs. G. Buechler, R. Gore, R. Mercer of Aerospace for valuable assistance in the project.



# Contents

	<u>Page</u>
I. Introduction . . . . .	1
II. Analysis of Satellite-to-Satellite Tracking . . . . .	3
2.1 Recursive Filter Simulations . . . . .	7
2.2 Inference Procedure . . . . .	10
2.3 Data Preparation . . . . .	10
2.4 Software Features and Modifications . . . . .	12
2.5 ATS Orbit Determination . . . . .	16
2.6 GEOS States . . . . .	18
2.7 Mass Distribution Location . . . . .	21
2.8 Normal Equations, Constraints. . . . .	23
2.9 Solutions to the Mass Layer . . . . .	25
2.10 Doppler Residuals . . . . .	35
2.11 Conclusions and Discussions. . . . .	39
2.12 Recommendation . . . . .	40
III. Altimetry Analysis. . . . .	41
3.0 Scope and Procedure . . . . .	41
3.1 Data Base . . . . .	42
3.2 Crossing Adjust . . . . .	42
3.3 Representation. . . . .	45
3.4 Remarks on Representation . . . . .	49
3.5 Truncated Kernel. . . . .	52
3.6 Mass Layer Regression. . . . .	53
3.7 Results . . . . .	56
3.8 Gravity Anomaly Differences. . . . .	60
3.9 Conclusions and Remarks . . . . .	62
Appendix I. Comparison of Disk and Point Mass Potentials at Depth. 1-1	
Appendix II. Potential and Attraction from a Disk . . . . .	2-1
Appendix III. Error Analysis of Truncated Kernel . . . . .	3-1
References . . . . .	R-1

## Figures

		<u>Page</u>
1.	Geometry of SST Tracking . . . . .	4
2.	Acceleration Output from Recursive Filter, True Unmodeled Accelerations . . . . .	8
3.	Earth Traces of SST Arcs . . . . .	13
4.	C-B Range Residuals, Laser Range Residuals. . . . .	22
5.	RMS Mass and RMS Doppler Residual vs $\sigma_a$ . . . . .	26
6.	Mass Layer Vertical Acceleration at 850 km Altitude ( $\sigma_a = .3 \times 10^{-7}$ earth). . . . .	31
7.	Mass Layer Vertical Acceleration at 850 km Altitude ( $\sigma_a = .5 \times 10^{-7}$ earth). . . . .	32
8.	Geographic Distribution of Mass Anomalies. . . . .	33
9.	Total Vertical Acceleration Sensed by GEOS (GEM-6 plus mass layer). . . . .	34
10.	Doppler Residuals for Rev 268. . . . .	36
11.	Doppler Residuals for Rev 926. . . . .	37
12.	Doppler Residuals for Rev 269. . . . .	38
13.	Earth Traces of Altimetry Passes . . . . .	43
14.	Stokes' and Inverse Distance Kernel . . . . .	47
15.	Geoid Difference Between Point and Disk Mass . . . . .	50
16.	Gravity Disturbance Difference Between Point and Disk Mass. . . . .	51
17.	Modified Point Mass Geoid Kernel vs $\psi$ . . . . .	54
18.	Geoid Heights from Mass Layer, Total Geoid . . . . .	57
19.	Mass Distribution from Geoid Residuals Relative to GEM-6 . . . . .	58
20.	Geoid Residuals for GEM-6 and GEM-6 Plus Mass Layer. . . . .	59

## Tables

		<u>Page</u>
1.	Summary of SST Data Passes . . . . .	14
2.	ATS Data Fit Statistics . . . . .	17
3.	Formal Statistics for Sample Case of GEOS Orbit Determination . . . . .	19
4.	Mass Locations and Values from SST. . . . .	28
5.	Summary of Altimetry Passes. . . . .	44
6.	Mass Solution from Altimetry, Depth = 55.5 km. . . . .	55
7.	Statistics of Mass Layer Solutions . . . . .	56
8.	Gravity Anomaly Differences . . . . .	61

## I. Introduction

The objective of the study reported herein is to infer the exterior gravitational field of the earth and the structure of the geoid from GEOS-C metric data. Of the many measurement types available, the scope of our effort is limited to two: satellite-to-satellite range and range rate tracking (SST) and radar altimetry. Initially, our intent was to couple together the dynamical effects of the field perturbations on doppler or range rate with the geopotential-induced geoid displacements sensed by altimetry to obtain a single consistent model. However, it soon became apparent that the coupling between the two data types was too weak to justify the complexity involved in the short arc method of analysis employed. Because of the weak coupling, the analysis effort separated naturally into two parts: inference of the long wavelength disturbances from SST and the fine structure geoid from altimetry.

The division was also fortuitous from a chronological standpoint. The SST tracking which was actually used occurred prior to June 28, 1975 and all of it became available by mid-1976. Many passes of altimetry were also available but the coverage over the test area was not sufficiently dense until the latter part of 1976. By that time the SST work was well underway.

Section II of the report concerns various phases of the SST analysis. A direct point-by-point estimate of gravity disturbances by means of a recursive filter with backward smoothing was initially attempted but had to be forsaken due to poor convergence (attributed to inadequate signal-to-noise ratio). The adopted representation consists of a more or less uniform grid of discrete masses at a depth of approximately 400 km from the earth's surface. The layer is superimposed on a spherical harmonics model, in this case GEM-6 (Ref. 1).

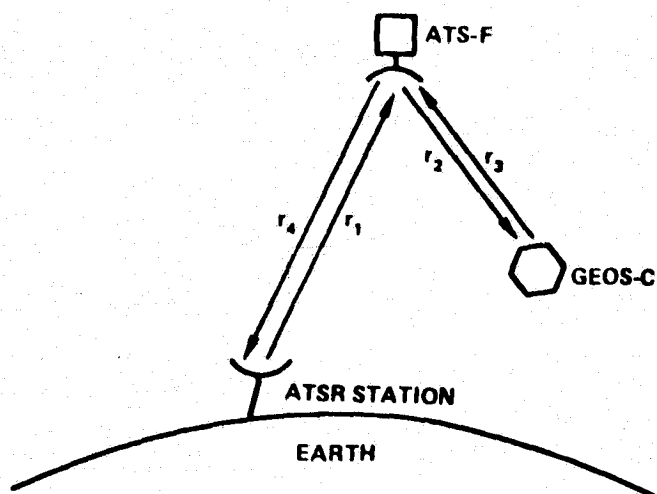
The second part of the report describes the procedure for smoothing the altimetry and inferring the fine-structured gravity field over the Atlantic test area. In place of the usual surface anomalies, we again chose to represent the local disturbances by means of a density layer. The altimeter height biases were first estimated by a least squares adjustment at orbital crossover points. The bias-adjusted data base contained 74 arcs with 6050 observations

and 1150 crossovers. After taking out the bias, long wavelength contributions from GEM-6 as well as a calibration correction from Reference 2 were subtracted. The residual heights were then represented by a mass distribution beneath the earth's surface.

## II. Analysis of Satellite-To-Satellite (SST) Tracking

The geometry of SST tracking is illustrated in Fig. 1. ATS-7 at synchronous altitude serves as a link between ground station and GEOS-C for range and doppler measurements. Two basically different approaches of analysis can be employed depending on the length of the data span. Some general comparative features are:

	Long Arcs Methods	Short Arcs Methods
a) Length of orbit/arc	Many revolutions (~100)/arc	Less than one revolution per arc
b) Number of arcs	Few - 3-4 over several months	Many - 50-60 over 2 months
c) Size of initial state vector	Small - 20-30	Large - 350
d) Aliasing	May be significant when data distribution is uneven	Adaptable to uneven data distribution, some absorp- tion of initial perturbations by state vectors
e) Sensitivity	More sensitive, particularly to long period perturbation	Sacrifices sensitivity to long wavelengths
f) Orbital dynamics	Favors dynamical theory for long term integration	Numerical integration applicable
g) Dynamical model	Orbital theory avail- able for harmonics, planets, solar pressure	Harmonics, discrete anomalies, and all modeled forces
h) Linearity	May be nonlinear unless one starts with good state vector	Very linear, usually con- verges in a single iteration with reasonably good initial states
i) Singularity	Nonsingular in states, may be near singular in harmonics	May be near singular in both states and gravitational param- eters. Some a priori informa- tion stabilization usually re- quired depending on coverage



$$\begin{aligned}\text{RANGE SUM} &= r_1 + r_2 + r_3 + r_4 \\ \text{RANGE RATE SUM} &= \dot{r}_1 + \dot{r}_2 + \dot{r}_3 + \dot{r}_4\end{aligned}$$

Figure 1. Geometry of SST Tracking

j) Computer time requirements/iteration	Not evaluated	Acceptable - 3200 sec/iteration on CDC 7600 for 716 parameters, 4310 observations; large part of time taken up in computing observations and observation partials
k) Accuracy	Adequate	Adequate down to less than .1 mm/sec

We chose the short arc approach for reasons of d, f, g, h, j above and also because of our past experience with the method in analyzing lunar and Mars orbiter data. Our inventory of software required relatively minor revisions. To summarize, the high degree of linearity, reduction of process noise (aliasing), numerical accuracy, simplicity, computer time economy, and software availability were the factors in our choice.

Having decided on a short arc technique, there are a number of considerations such as the filtering algorithm, data types to analyze, and the method of representation. Initially our intent was to combine SST with ground tracking, i. e., doppler, C-band, laser, together with altimetry to obtain a single consistent solution. Each element of the disturbing potential,  $T$ , would produce an acceleration  $\nabla T$  on the motion of GEOS-C sensed by the various tracking systems. It would also cause a height anomaly,  $\Delta N = T/Y^*$ , measurable by altimetry and a gravity anomaly,  $\Delta g = -\frac{\partial T}{\partial r} - \frac{2T}{r}$ , derivable from surface data. The plan is ideal in principle and might be amenable to analysis utilizing a long arc approach. For short arcs, the combination of the data types is unnecessarily complicated. Since GEOS is at an altitude of 850 km, one would not expect its orbit to be sensitive (over time spans of a half revolution) to disturbances with wavelengths, much less than twice the altitude. Since the orbit perturbations are sensing features with  $\lambda$  on the order 2000 km, perturbations arising from fine structure variations of few tens kilometers as measured by the altimeter would be entirely lost in the noise. There was no need to add the altimetry to the SST data in a short arc analysis. Decoupling simplified the problem considerably.

There is next the question of a filter or smoothing algorithm for the SST. Some possible choices are: 1) arc by arc polynomial spline fits of doppler data residuals which are based on a low degree harmonics model followed by analytical differentiation to obtain point accelerations, 2) point by point estimate of unmodeled accelerations with a recursive filter--also one arc at a time, 3) directly fitting to all selected arcs by means of a set of discrete parameters (may be harmonics coefficients, density elements, surface anomalies, or geoid heights).

---

\*  $Y$  is normal gravity and  $r$  is the radial coordinate.



The Jet Propulsion Laboratory has applied the first extensively to the tracking of lunar, orbiters, Apollo and GEOS [1, 2, 3]. Only limited application of the second has been made [4, 5]. The last is the one used on the Moon and Mars [6, 7]. The principal differences between the first two and the third is that, in the former, accelerations are derived directly from the data and the sources can be inferred by means of a static (nondynamical) fit at a later time. The advantage of the third method over the first is that aliasing, where a part of the gravitational signal residuals may be absorbed by the states in the initial fit with a low degree model, is reduced by estimating state and field parameters simultaneously. In principle, method 2 is the most attractive because it combines simultaneous state and unmodeled-acceleration estimation with the possibility of static fit. The latter feature is so important that we decided to examine the feasibility of filtering in some detail by means of a simulation study for possible application to the analysis of the SST tracking.

## 2.1 Recursive Filtering Simulations

The steps in the filter simulations were as follows:

- a) Generate range and range rate observations from ATS and GEOS using a dynamical model containing small gravitational disturbances (on the order of 1-10 milligals at GEOS altitude) superimposed on a low degree field. Zero means Gaussian noise with standard deviation of 1 meter and 1 mm/sec, respectively, were added to the generated data.
- b) A forward and backward (or smoothing [8]) recursive filter with plant noise compensation was applied to the generated data to estimate the unmodeled accelerations. The filter dynamics contained the nominal harmonic field plus the filtered accelerations. At each time point,  $t_i$ , the forward and backward filter outputs were combined to obtain a minimum variance estimate including the effects of both data before and after  $t_i$ .

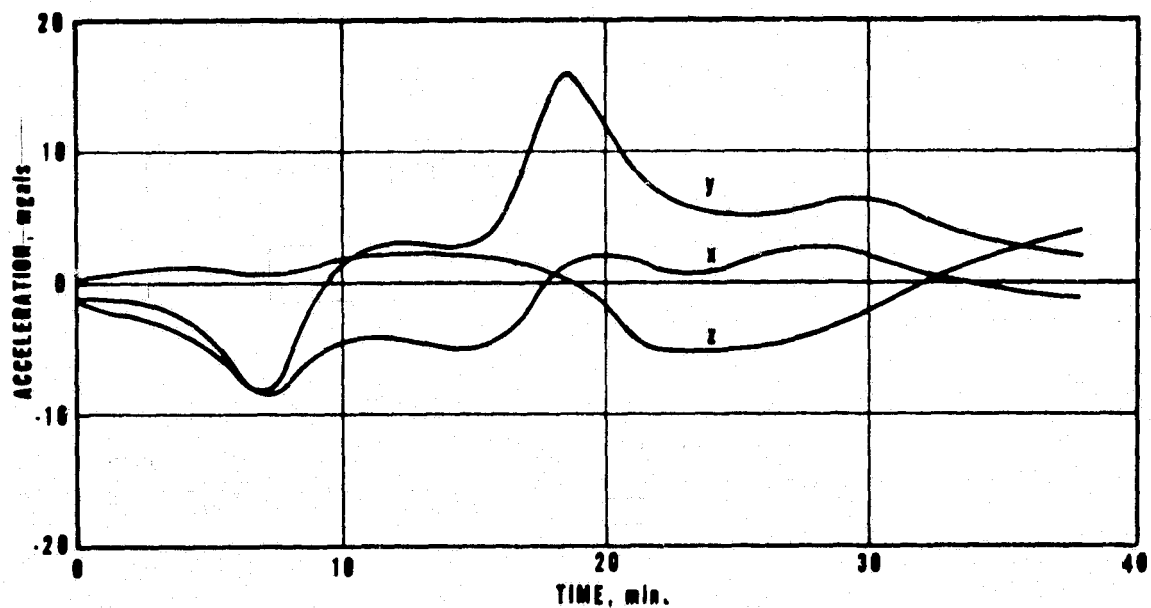


Fig. 2a Acceleration Output from Recursive Filter

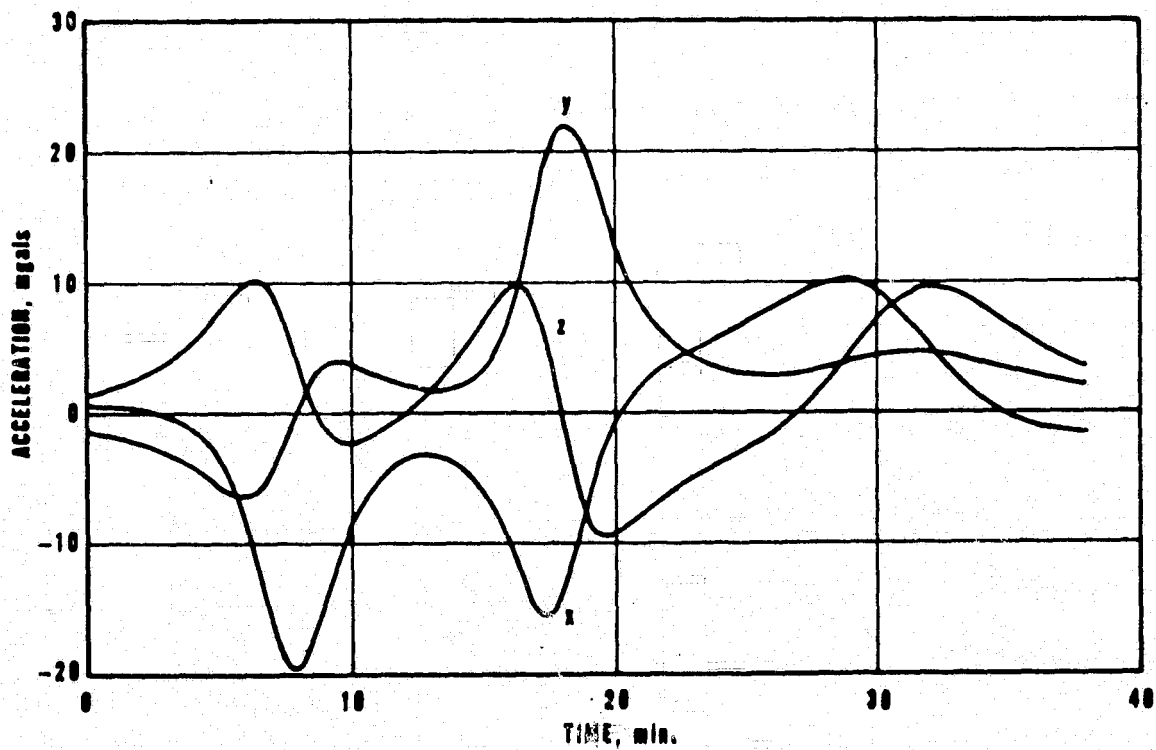


Fig. 2b True Unmodeled Accelerations

Differential equations for the filter are:

$$\dot{\mathbf{x}} = \mathbf{v} ; \quad \dot{\mathbf{v}} = \mathbf{a} + \mathbf{u} ; \quad \dot{\mathbf{u}} = -\beta \mathbf{u} + \boldsymbol{\theta}$$

where  $\mathbf{x}$ ,  $\mathbf{v}$ ,  $\mathbf{a}$ , and  $\mathbf{u}$  are 3-vectors of position, velocity, modeled acceleration, and unmodeled acceleration, respectively.  $\boldsymbol{\theta}$  is a zero mean Gaussian process with given covariance,  $\beta$  is a reciprocal time constant. Parameters varied in the simulation included a priori variances on the states,  $\beta^{-1}$ , plant noise level. A wide range on the parameters were tried:

<u>Parameter</u>	<u>Range</u>
$\sigma(\mathbf{x})$	5 - 1000 meters
$\sigma(\mathbf{v})$	.005 - 1 m/sec
$\sigma(\mathbf{u}_0)$	1 - 10 mgals
$\beta^{-1}$	100 - 1000 seconds
$\sigma(\boldsymbol{\theta})$	$10^{-2}$ - 3 mgals over 10-40 second interval

Initially, the unmodeled acceleration was limited to about 2 mgals maximum amplitude. The filter results were disappointing. When  $\sigma(\boldsymbol{\theta})$  was very small, say  $10^{-2}$  mgals, (approximate random part of the field over a 10 second span) a posteriori  $\sigma(\mathbf{u})$  was on the order of .05 - .1 mgals for values of  $\beta^{-1} \simeq 500$  seconds, ( $\beta$  was held fixed). Increasing  $\sigma(\boldsymbol{\theta})$  to .2 mgals increased  $\sigma(\mathbf{u})$  to a range of .5 - 3 mgals. The latter is certain to be too large. In either case, the filter output deviated from the correct answer by an unacceptably large amount--from a few tenths to as much as 10 mgals. The results were not altogether unreasonable since two observations over a 10 second interval could, at best, measure acceleration along the line-of-sight to say .14 mm/sec<sup>2</sup>  $\simeq$  14 mgals. With such a low signal to noise ratio, a lengthy smoothing time (or large value of  $\beta^{-1}$ ) was needed and the random component cannot be assumed correlated over times much greater than, say, 100 seconds. An experiment in which the perturbation level was increased ten fold (to a maximum of 20 mgals) was also made. A typical output is shown in Fig. 2a which should be compared

with the true values shown in Fig. 2b. The figures have some resemblance to each other, but are clearly too far apart for the level of accuracy being sought. The recursive method would undoubtedly be more appropriate for the Moon or Mars where anomalies on the order of several hundred milligals are present. In the case of the earth, a measurement noise level of 1 mm/sec appears too high for detecting the small signals at GEOS altitudes by filtering.

## 2.2 Inference Procedure

Having forsaken the filtering approach, we reverted to the method of representation by discrete elements, in this case point masses. The object is to infer a mass or density layer by fitting to the doppler observations. In the case of SST tracking under consideration, an outline of the steps in the inference procedure is as follows:

- a) Select the data base for ATS and GEOS. Edit and presmooth data, separate into individual passes of about one hour duration.
- b) Determine accurate ATS ephemeris from data base and update to GEOS tracking periods.
- c) Obtain preliminary GEOS states at beginning of each pass. Adjust states to obtain best fit of SST tracking using model which includes all significant forces except residual gravity disturbances. Each arc is adjusted separately.
- d) Establish grid of mass point coordinates. Generate partial derivatives of doppler observations with respect to mass magnitudes and the six initial states. Starting with those from step c, the partials are generated one arc at a time.
- e) Form normal equations and solve to find improved states and masses under constraints.
- f) Iterate to convergence.

## 2.3 Data Preparation

Much of the preliminary work was related to decoding, presmoothing, editing and reformatting of the data tape. A program was written to perform

all four functions and punch cards in a format acceptable by the Aerospace orbit program as output. In addition to station code, time, and smoothed measurement, each card also contained frequency synthesizer mode codes to enable calculation of appropriate scaling constants for the doppler count. Approximately 7500 smoothed observations were selected, 3000 ATS and 4500 GEOS, representing 12000 and 18000 uncompressed 10 second samples for ATS and GEOS, respectively.

### Pre-Smoothing and Editing

Computation of the observable, i. e., the doppler count and its partial derivatives, consumed a substantial part of the time for the regression because of the tedious iterative algorithm involving five range legs at the beginning and end of each count interval. To conserve time, each frame of four 10 second points was compressed into a single smoothed point by means of a quadratic polynomial. A cubic could also be used but the cubic yields exactly the same value at the midpoint as a quadratic with the difference that the residuals are zero. The quadratic was used since it was simpler and because the residuals from the second degree fit provided a means for the initial editing of outliers (of which there were a significant number, particularly near the extremities of a pass). In principle, the smoothed values should have a smaller noise variance but the reduction is quite small--on the order of 20 percent for the standard deviation. The main purpose is that the 40 second sampling rate reduced computing time by a factor of four with hardly any sacrifice in sensitivity.

Refraction induced residual tails were very much in evidence for all the long passes where the ray path traversed the ionosphere. Since modeling of the refraction profile was not one of our objectives, the first and last few minutes of data in each pass were dropped. The earth central angle,  $\theta$ , between ATS and GEOS served as a quantitative rejection criterion. Observations for which  $\theta$  exceeded 95.5 degrees were deleted. The cutoff value corresponds to a minimum altitude of 600 km for the ray path.

A similar data compression scheme was applied to ATS. The loss of sensitivity is even less in the case of ATS.

## Data Base - GEOS

The original data tapes contained about 176 passes taken over the period from 16 April to 26 June 1975. Since the GEOS altitude was  $\sim 850$  km, we wanted to select passes with an equatorial longitude spacing on the order of the altitude or slightly less than 8 degrees. Forty five passes would cover the entire circumference and 90 would suffice to include both ascending and descending geometries. The actual passes fell far short of the desired coverage. Much of the Atlantic had redundant passes while the Pacific was not included at all (such an uneven distribution tends to favor a discrete or mass layer representation over a spherical harmonics expansion). In the process of selecting the passes to be used in our solution, we examined nearly every pass available as to quality, geometry, and coverage. A total of 59 passes were included in the final data base. Figure 3 shows the geographic distribution of the pass while Table 1 summarizes some pertinent statistics. The average number of points (nominally 40 seconds apart) per pass is 73 and the average duration about 50 minutes.

The pass geometry may be graded by the minimum value of  $\theta$ ,  $\theta_{\min}$ . Passes with  $\theta_{\min} \leq 50$  degrees comprise about 75 percent (44 passes). The remainder have  $\theta_{\min}$  between 50 and 65 degrees. It should be mentioned that  $\theta$  ranges from about 95.5 degrees to  $\theta_{\min}$  on all the passes, i. e.,  $\theta$  is at or near  $\theta_{\min}$  (the vicinity where the doppler data has the maximum sensitivity to anomalies) only over a fraction of the pass (see next section).

The coverage of the earth by good geometry passes is far from complete, even for the regions from -100 to +100 longitude--but we are unable to fill in any more gaps from the data tape currently available. Many of the candidate passes in early May either were too noisy or had dropouts during the crucial segments when the sensitivity is near the peak.

### 2.4 Software Features and Modifications

The principal analysis tool is a modified version of the Aerospace orbit program, TRACE. The program numerically integrates the dynamical equations, including effects of sun, moon, geopotential, and radiation pressure

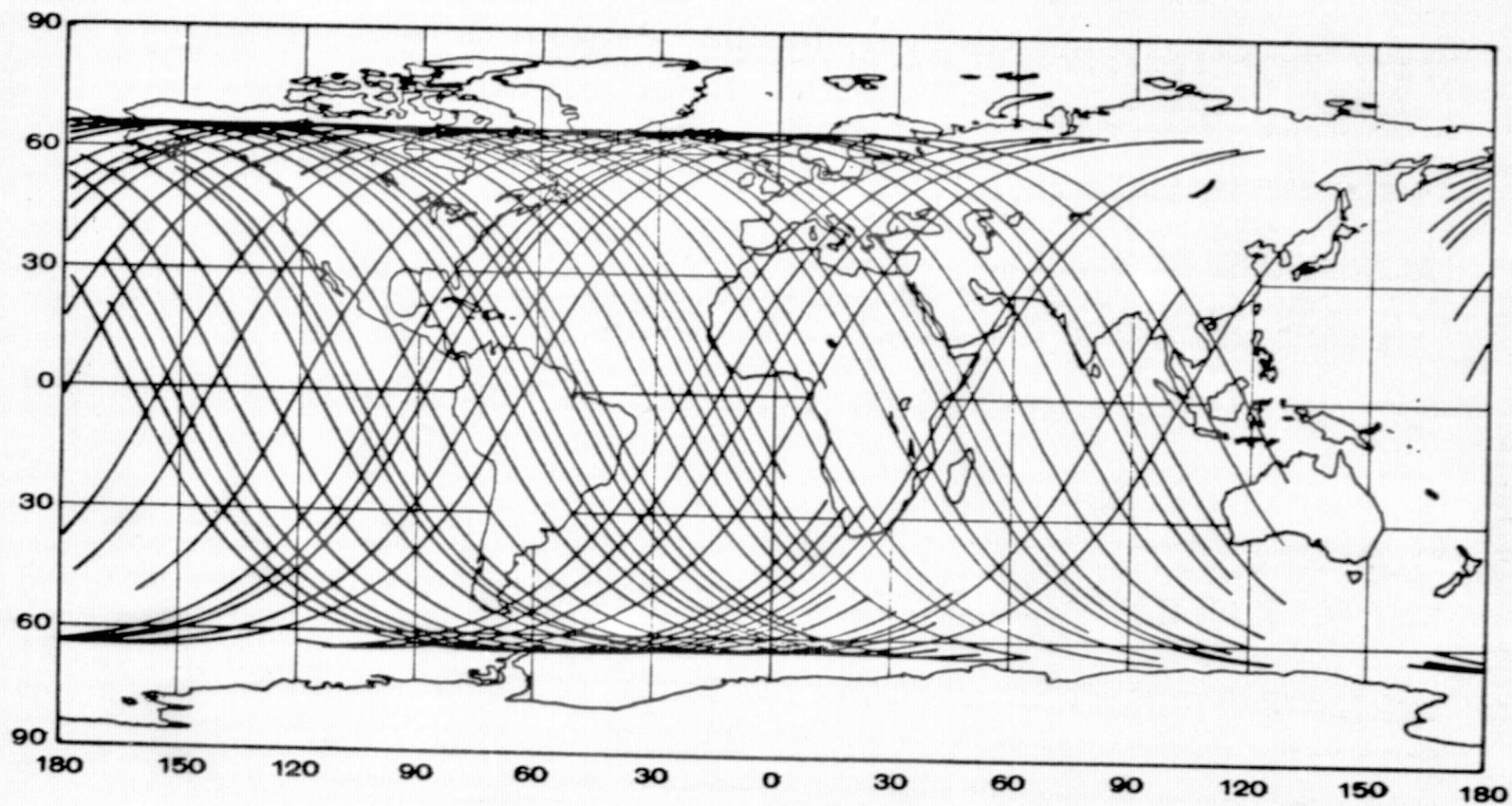


Figure 3. Earth Traces of SST Arcs

Table 1. Summary of SST Data Passes

Start					Stop		THETAMIN	NOCE	AS	ST	NPT	*
REV	MN	CA	HF	MIN	HR	MIN						
22												

\*YEAR = 1975, MN = month, DA = day, HR = hour, THETMIN = Minimum earth central angle from ATS to GEOS, NODE = east longitude in degrees; AS, A = ascending, D = descending; ST, 58 = Rosman, 99 - Madrid, NPT = number of 40 second samples.



(for ATS only) in an inertial coordinate system, as well as the variational equations for parameters being estimated. Both trajectory and variational equation solutions are interpolated at observation times which are intermediate to integration step times. A subroutine then computes the value of the observations and partials from the interpolated states for the differential correction routine. Some relevant properties of the program for this application are:

- a) Coordinate system - Integrates in inertial coordinates; equator, equinox at midnight of date, outputs in equator and equinox of date.
- b) Time - Integration time is uniform, output time is UTC, linear equations relate integration time to UTC, UT1, and ephemeris time.
- c) Geopotential - Includes dynamical and variational equations for spherical harmonics as well as discrete masses.

Some pertinent constants for the analysis are:

Earth model for GEOS	- Full GEM-6 with 174 pairs of terms, Ref [9]
ATS	- GEM-6 truncated at degree 6
Earth radius	- 6378145 meters
Flattening	- $(298.255)^{-1}$
GM	- $3.986008 \times 10^{14} \text{ m}^3/\text{sec}^2$
Velocity of light	- $2.997924562 \times 10^8 \text{ m/sec}$ NBS (1972)
Station coordinates	- Best available locations from Mr. J. Marsh of GSFC

Major modifications for the present analysis task included:

- a) Range and range rate equations for satellite-to-satellite tracking
- b) Range trilateration equation for ATS
- c) Variational equations for SST with respect to geopotential parameters which had to be expanded to accommodate 362 point masses plus 6 initial states

- d) Frequency synthesizer equations to calculate constants for scaling the range differences into doppler count.

A considerable part of the TRACE work involves expanding of sub-routines to accommodate the integration of some 362 sets of variational equations for the mass grid. The range and range rate algorithms, frequency synthesizer equations are given in informal notes from NASA Ref. [10]. Ambiguity resolution of both the doppler count and range rollover are done in TRACE with the aid of an initial orbit.

## 2.5 ATS Orbit Determination

Even though the preliminary analysis indicated that the ATS status could be observed in idealized geometry cases from a single pass of SST data, the fact that ATS state errors of several kilometers and 10's of mm/sec had little effect on the gravity estimates prompted us to fix the ATS states in the gravity solution thus eliminating a potential source of singularity--particularly in cases with degraded geometry. It was inconvenient to use the NASA furnished ATS initial states due to probable differences in coordinate system, time, and dynamical model. Hence, it was decided to determine the ATS orbits from the observations supplied. The results would also serve as a check on our algorithms and software.

The tracking data on ATS from 4/27 to 6/28/75 were divided into seven arcs whose length varied from about 3 to 10 days. Care was taken against having a maneuver within any segment. We estimated six state parameters, a radiation pressure constant,  $Y$ , and a number of range bias parameters in each arc to fit range and range rate. In contrast to the gravity inference, the range measurements contribute much more towards establishing the ephemeris than the doppler. An average value of  $Y = .727 \times 10^{-7} \text{ kg/m}^2$  was obtained over the two month period. The number of bias parameters depended on the data included in the span. A parameter was introduced whenever one was indicated either from the tracking notes sent with the ATS tape or from the residual patterns. Some statistics on the ATS ephemeris determination are given in Table 2.

Table 2. ATS Data Fit Statistics

Start Time		Stop Time		Stations*	RMS Residuals	
Month	Day	Month	Day		Range - m	Doppler - h <sub>z</sub>
4	27	5	4	R, S, Me	2.9 (245)**	.010 ( 35)
5	11	5	20	R, Me	11.2 (724)	.0048 (384)
5	22	5	30	R, Me, Md	14.8 (618)	.0086 (324)
5	31	6	8	R, Md	19.1 (381)	.023 (239)
6	11	6	20	A, Md	11.1 (373)	.0059 (245)
6	21	6	24	A, Md	8.5 (285)	.020 (139)
6	25	6	28	A, Md	6.8 (299)	.0059 ( 46)

\*R = Rosman, Me = Mojave, A = Ahmedabad, Md = Madrid

\*\*Number in parenthesis = number of smoothed observations

Systematic trends were evident and the fits could be improved by adding more bias parameters. In one experiment on the first arc, we achieved an RMS of .8 meters over 1032 range measurements by introducing 34 bias parameters. Assuming a measurement standard error of 1 m on each observation, the formal statistics indicate 1 sigma uncertainties of:

$$\sigma(\text{Range bias}) \simeq 15 \text{ meters}$$

$$\sigma(\text{Position}) \simeq 150 \text{ meters}$$

$$\sigma(\text{Velocity}) \simeq 1 \text{ cm/sec}$$

The converged state vector difference between the orbit with the many bias parameters (and small RMS residual) and the one with just a few biases and poorer fit was about 1 km in position and 5 cm/sec in velocity. It was felt that the biases remaining did not alter the ATS ephemeris enough to affect the short arc solutions. Hence, the later arcs had fewer bias parameters in the estimations and poorer RMS fit.

After the solutions converged, the ATS ephemeris had to be updated to epochs just prior to the start of each GEOS arc. They were subsequently held fixed for analysis of the SST data. Comparisons of our ephemeris with the ones given in the NASA tracking notes indicate differences of a few kilometers and several cm/sec which should be adequate. Preliminary covariance analysis indicates that the ATS errors resulting from estimation along with the GEOS states in a short arc mode using the SST tracking would be on the same order.

## 2.6 GEOS States

Considerable effort was expended in preliminary experiments with GEOS orbit determination. Most of the trial runs relate to combining data from various sensors, i.e., C-band, laser, and SST. The objective was to see how much ground tracking contributes in improving observability of orbit and gravity field parameters. Since our plan included analysis of altimetry data at the time, the accuracy of GEOS altitude was also of particular interest. A summary of an example pass on 27 April 1975 is given in Table 3. This pass contained some simultaneous C-band, laser, and SST tracking. The latter extended from 29670 to 33010 sec GMT and was classed as good pass geometry ( $\theta_{\min} \approx 30$  degrees, cf Sec. 2.3). In this run we included C-band tracking from a prior rev as well as the one coincident with the SST. Both C-band and laser were of excellent quality. Typical laser residuals are shown in Fig. 4. The RMS residuals were as low as .15 m. Formal statistics from various data combinations listed in Table 3 revealed some pertinent and more or less expected results:

- a) Ground tracking is better than SST doppler in determining GEOS ephemeris even if one assumed perfect ATS ephemeris along with the latter data.
- b) If one combined ground tracking with SST and estimated ATS and GEOS states, then the GEOS state errors are about the same as the ones in case 3, i.e., ground data alone, but the ATS ephemeris is no better than about 1600 meters. Hence, little is gained by trying to improve the ATS orbit with ground and SST tracking on GEOS.

Table 3. Formal Statistics for Sample Case of GEOS Orbit Determination

<u>Initial GEOS State</u>	Nominal	<u>Standard Deviation (<math>\sigma</math>) of GEOS States</u>					<u>ATS States</u>	
Epoch = 1975, April 27, 7 <sup>h</sup> 0 <sup>m</sup>	<u>States</u>	<u>Case 1</u>	<u>Case 2</u>	<u>Case 3</u>	<u>Case 4</u>	<u>Case 5</u>	<u>Case 2</u>	<u>Case 5</u>
Right ascension ( $\alpha$ ) - deg	281.092	.15E-5	.44E-5	.44E-5	.38E-4	.0052	.0013	.0039
Declination ( $\delta$ ) - deg	10.751	.20E-5	.65E-5	.70E-5	.11E-3	.0033	.0022	.024
Velocity angle from vertical ( $\beta$ ) - deg	90.023	.23E-5	.12E-4	.15E-4	.30E-5	.00010	.0030	.020
Inertial azimuth (A) - deg	334.541	.28E-5	.90E-5	.90E-5	.11E-3	.0028	.0017	.019
Radius (r) - meters	7219705.	.12	.80	.96	.64	69	1580	9040
Velocity (v) - m/sec	7433.811	.120E-3	.82E-3	.99E-3	.59E-3	.050	.039	.16

<u>Case</u>	<u>Data in Fit</u>	<u>Regression Parameters</u>	<u>Rank</u>
1	CB, L, SST	G + 8 biases	6
2	CB, L, SST	G + A + 8 biases	12
3	CB, L	G + 8 biases	6
4	SST	G	6
5	SST	G + A	9

Notes:

1. CB = 2 C-band trackers, L = 2 laser stations, SST = doppler only (too few range points which also appeared biased).
2. G = 6-vector of GEOS states, A = 6-vector of ATS, 8 biases are range, azimuth, elevation for each C-band and range for each laser.
3. Pass was on 1975, April 28, 8<sup>h</sup> 14<sup>m</sup> to 9<sup>h</sup> 10<sup>m</sup>, rev 245/246.

- c) SST data by itself should not be used to simultaneously estimate ATS and GEOS ephemeris. Uncertainties in ATS of almost 2 km are incurred even with a reduced rank solution, in this case rank = 9.

While these runs showed the importance of ground tracking in establishing the ephemeris, it was clear that the levels of accuracy obtainable with the SST data alone was adequate for sensing the gravity disturbance field. Also, previous covariance analysis indicated that little is to be gained from the 1m range tracking in sensing the small gravity disturbances. Very accurate doppler tracking from the ground would be of use but a search of the data catalog revealed very limited simultaneous tracks with SST. Furthermore, the tracks are limited in time duration and coverage. In view of the small return for labor expended, we decided to use only SST tracking for the gravity solution with fixed ATS states derived from ground based range tracking. This procedure simplifies the problem by eliminating some  $59 \times 6 = 354$  ATS state parameters from the linear system.

The GEOS states we started with were obtained from converged orbit determination fits to the SST doppler using TRACE with sun, moon, and full GEM-6 geopotential. Each arc of about 50 minutes determines a separate set of states. Starting values came from the NASA tracking notes extended to the initial epoch of each arc, also using the GEM-6 model. These initial runs served to edit outliers and the pass tails affected by refraction. Passes with biases, discontinuities, poor or redundant geometry were thus eliminated. The small remaining residuals from these runs indicated a low signal to noise ratio with the GEM-6 model as base harmonics. Reruns on several passes using SAO 73 were made. The signatures were higher but still quite low.

The excellent fit of the data with GEM-6 is a mixed blessing. The small magnitude of gravity error means that there will be very little aliasing between initial state and gravity model error. It also means that the corrections to the model and state will be highly linear because of small amplitudes. On the minus side, it means that we will be hardpressed to improve on the model unless the observation noise level is low enough to reveal some definitive

signature. All of our preliminary orbit determination runs show that the best we can hope for is about a 2 to 1 reduction in RMS and the final runs show that it is considerably less than 2 to 1.

Most of the runs converged in 2 to 3 iterations from the initial states with RMS doppler residuals of about .01 Hz. Typical statistics are given in case 4 of Table 3.

## 2.7 Mass Distribution Location

In using a mass layer representation, choices must be made on the density of grid points, geographic location, and the extent of the layer if non-global. We wanted to extend the distribution such that the distances from GEOS to the most remote mass is at least 5 times the distance to the closest mass (which is in the vicinity of the subsatellite point) so that the acceleration magnitude for the former is reduced by a factor of about 25. At an altitude of 850 km the lateral distance should be about 40 deg. From the coverage shown in Fig. 1, with the 40 deg extension on each side, there is little uncovered area remaining. On this basis, we decided that the layer may as well extend over the entire earth when all the arcs are analyzed simultaneously. A complete layer allows the easy imposition of certain linear constraints to the density solution.

Our rule-of-thumb for grid point separation is that it should be about equal to the vertical distance to GEOS. If the masses are located on the surface, the separation should be about 850 km. The initial thought was to use  $10^\circ \times 10^\circ$  equal area squares which number 410 with a spacing of 1110 km. However, the grid has some asymmetries which could cause distortions when the low-degree harmonic constraints are applied (see Sec. 2.8). The actual grid chosen is a subdivision of an icosahedron with a total of 362 points. Each of the 20 faces has an identical grid point pattern. The average distance between points is ~1270 km. By choosing the radius of the layer to be 5950 km (depth 425 km), the mean altitude to GEOS is also about 1270 km. Table 4 which contains the mass values from the final solution also lists all of the grid point latitudes and longitudes. The 10 reference vertices are located at the north and south pole;  $26.565^\circ\text{N}$ ,  $n72^\circ\text{E}$ ,  $26.565^\circ\text{S}$ ,  $(n72 + 36)^\circ\text{E}$ ; where  $n = 0$  to 4.

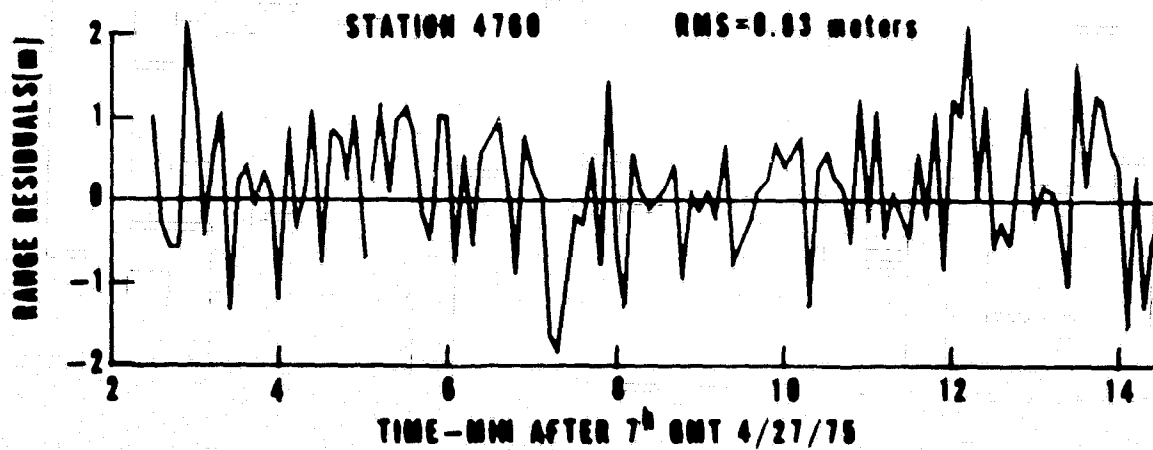


Fig. 4a Typical C-Band Range Residuals

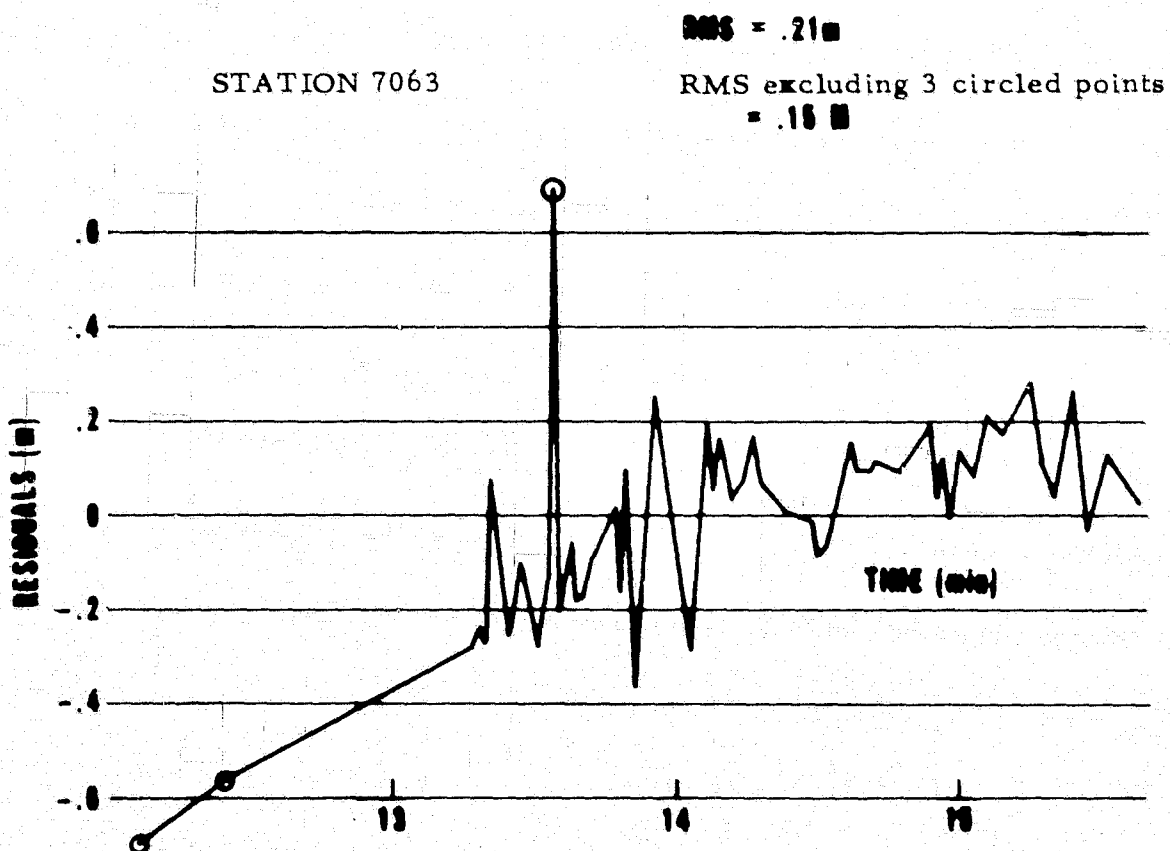


Fig. 4b. Typical Laser Range Residuals



## 2.8 Normal Equations, Constraints

In this section we use the notations:

- O - n vector of observations; n = 4310
- x - m vector of parameters to be estimated; m = 716
- W - Matrix of observation weights, generally assigned to be reciprocal variance of each observation
- A - n x m matrix of partials,  $A = \frac{\partial O}{\partial x}$ ,  $A' = A$  transpose
- b - n vector of residuals (observed minus calculated)

In order to minimize the quadratic sum  $S = b'Wb$ , we solve the linear system

$$N = (A'WA + \Gamma^{-1}) x = A'Wb \quad (1)$$

where  $\Gamma$  is the covariance of the initial estimate,  $x_0$ . The new estimate is  $x_0 + x$  and the covariance matrix is  $(A'WA + \Gamma^{-1})^{-1}$ . The matrix N is accumulated and stored as the submatrices  $A_i$  for the  $i^{\text{th}}$  arc are generated individually. The vector x consists of 354 initial states (6 each for 59 arcs) and 362 mass parameters.

One of the shortcomings of the discrete mass representations is that it tends to distort the low degree harmonics. Since short arc solutions are only slightly sensitive to these harmonics, it was decided to impose constraints on the solution such that the low degree harmonics would be invariant from the GEM-6 solution. We set the limit at 4, i.e., the mass layer obtained from solving (1) should contain no harmonics of degree 4 or less nor zonal harmonics through degree 15. The constraint equations may be expressed as:

$$\sum_{i=1}^{362} \Delta m_i K_{\ell}^m(\phi_i, \lambda_i) = \sum_{i=1}^{362} m_{i0} K_{\ell}^m(\phi_i, \lambda_i) \quad \begin{array}{l} \ell = 0, 1, 2, 3, 4 \\ m = 0 \dots \ell \\ \ell = 5, 6, \dots, 15 \\ m = 0 \end{array} \quad (2)$$

where  $K_{\ell}^m(\phi_i, \lambda_i)$  are the surface harmonics of degree  $\ell$ , order  $m$  evaluated at the  $i^{\text{th}}$  mass latitude  $\phi_i$  and longitude  $\lambda_i$ ,  $\Delta m_i$  are the changes in mass from solving equation (1) and  $m_{i0}$  is the initial value of the  $i^{\text{th}}$  mass. For example, when  $\ell = m = 0$  the condition is simply

$$\sum \Delta m_i = - \sum m_{i0} \quad \text{or} \quad \sum \Delta m_i + \sum m_{i0} \equiv 0$$

or that the total mass of the layer is zero, thus maintaining the starting value of GM. When  $\ell = 1$ ,  $m = 0$

$$\sum \Delta m_i Z_i = - \sum m_{i0} Z_i$$

the Z coordinate of the center of mass remains fixed, etc. To impose the constraints listed above requires 36 equations, thus effectively reducing the rank of the linear systems to 680. Using Morrison's method, we let  $x = By + r$  where B is a 716 x 680 constraint matrix, x is arranged so that the 362 masses precede the 354 states and the first 36 masses will be dependent parameters. We solved the reduced system:

$$B'NBy = B'(A'Wb - Nr) \quad (3)$$

The constraint (2) may be expressed in matrix rotation as

$$(C_1 \ C_2) \begin{pmatrix} x_1 \\ x_2 \end{pmatrix} = \alpha \quad (4)$$

$C_1$  is an invertible 36 x 36 square matrix,  $C_2$  is 36 x 326,  $\alpha$  is 36 x 1;  $C_2$  is just the right side of equation (2). Solving for  $x_1$  from (4),

$$x_1 = C_1^{-1}(\alpha - C_2 x_2)$$

Identifying  $x_2$  as the independent variables y, the matrix B has the form

$$B = \begin{pmatrix} -C_1^{-1}C_2 & 0 \\ I_1 & 0 \\ 0 & I_2 \end{pmatrix} = \begin{pmatrix} B_{11} & 0 \\ B_{21} & 0 \\ 0 & B_{32} \end{pmatrix}$$

where  $B_{11} = -C_1^{-1}C_2$  has dimensions of  $36 \times 326$ ,  $B_{21} = I_1$  is the identity of dimension 326 and  $B_{32}$  is the identity of dimension 354,  $r$  is a column vector whose first 36 elements equal  $\alpha$  and the remaining elements are zeroes. Equation (3) can now be solved for  $y$  from which  $x$  follows.

The method was applied to Mariner 9 analysis and was revived for the present application due to the similarity of the problems.

## 2.9 Solutions to the Mass Layer

The starting value of the masses were set at  $10^{-12}$  earth masses so as not to disturb the already converged state vectors. Using GEM-6 as the base model, the RMS residuals for the various arcs ranged from .0055 to .013 Hz with an average of .0094 Hz before the mass solution. The very low residual level indicates that the masses should be small (nominal noise level is .0075 Hz and this was the input value for data weights). While much larger anomaly induced signatures could be obtained by using a lower order (say 2,0 or 6,6) model as base, thus resulting in larger mass values, we chose GEM-6 to start from for the following reasons:

- We wish to evaluate the amount of signal not represented by GEM-6
- Since so much of the anomalous gravity power is already in the base model, the initial states will be only very slightly corrupted by model errors and, hence, closer to the correct solution. This means that the functions should be more linear and fewer iterations are required in comparison to a simpler base model. Our experience strongly dictates that a single iteration is all that's necessary.

The solution to the mass values were not uniquely determined because of incomplete coverage and the weak signal level. The mass magnitudes depended on the assigned a priori standard deviation,  $\sigma_a$ . As the a priori value is raised, the total RMS mass increased while the RMS data fit decreased. The variations are illustrated in Fig. 5.

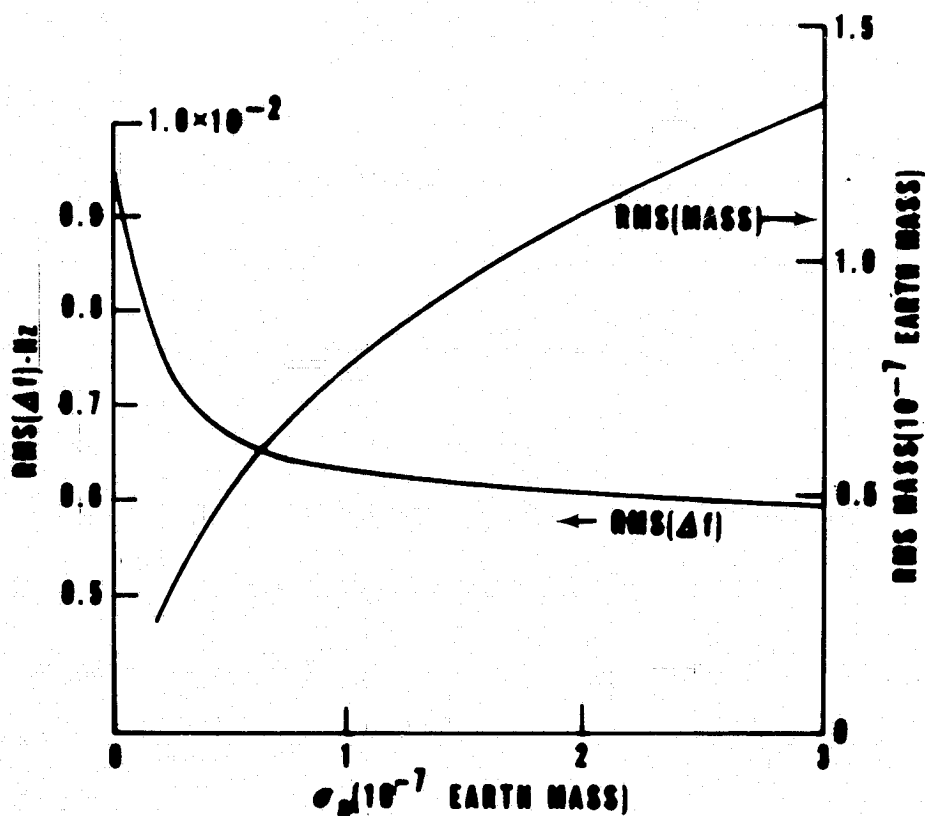


Figure 5. RMS Mass and RMS Doppler Residual vs  $\sigma_a$

A decision had to be made on the level of  $\sigma_a$ . One would like to obtain a small RMS mass along with small residuals. The asymptotic behavior of both curves in Fig. 5 indicates that the a priori should be set in the range of about  $.3 \times 10^{-7}$  to  $.5 \times 10^{-7}$  earth mass. Examination of the gravity disturbance plots of Figs. 6 and 7 reveals that the acceleration patterns are consistent i.e., the highs, lows, and zeroes all remain in place, but the magnitudes change. Furthermore, over the regions of good coverage, the actual disturbances vary considerably less than the ratio of .3 to .5 which is also encouraging. Fig. 5 shows that the RMS doppler residual decreases almost exponentially.

At  $\sigma_a = .3 \times 10^{-7}$  earth mass, 63.2 percent ( $1 - 1/\epsilon$ ) of the total decrease had been achieved. A further increase of  $\sigma_a$  to  $.5 \times 10^{-7}$  em attains a net decrease in RMS of 13 percent (of the total change) but increases the RMS mass by almost 45 percent with most of the large changes outside the regions of good coverage. We therefore adopted the case with  $\sigma_a = .3 \times 10^{-7}$  as our best solution and ascribe an uncertainty corresponding to the differences between solutions. Over the regions of good coverage, the gravity disturbances differ by about .3 to .5 mgals.

Some statistics on the final solution are:

Number of arcs	59
Number of observations	4310
RMS doppler residual (pre)	.0094
RMS doppler residual (post)	.0070
Mean mass	-.37 E-16 earth (constrained to be zero)
RMS mass	.36E-7
Formal standard deviation of each mass	.18 to .28E-7

Since a unit ( $10^{-7}$  earth mass) causes a maximum of 2.6 mgals at GEOS altitude, the gravity disturbances are on the order of 1 or 2 milligals. A tabulation of the magnitude and locations are given in Table 4. Each point is located at distance 5950 km from the geocenter. The points are geographically displayed in Fig. 6 where the numeral locates the surface coordinate and the values are in units of  $10^{-8}$  earth mass.

A contour plot of the vertical component of gravity disturbance at 850 km is shown in Fig. 9 representing contributions from the mass layer plus GEM-6. The contour interval is 4 mgal with K as the zero level. Since the GEM-6 contours are 10 times the contours from the mass layer, Fig. 9 is very close to the contours of GEM-6 by itself.

It should be mentioned that what is plotted are accelerations and not gravity anomalies. A positive or mass excess causes a negative acceleration, i. e., an acceleration along the negative radial direction. (This is opposite in sign to the usual anomalies where a positive mass causes a positive anomaly.)

208

REPRODUCIBILITY OF THE  
ORIGINAL PAGE IS POOR

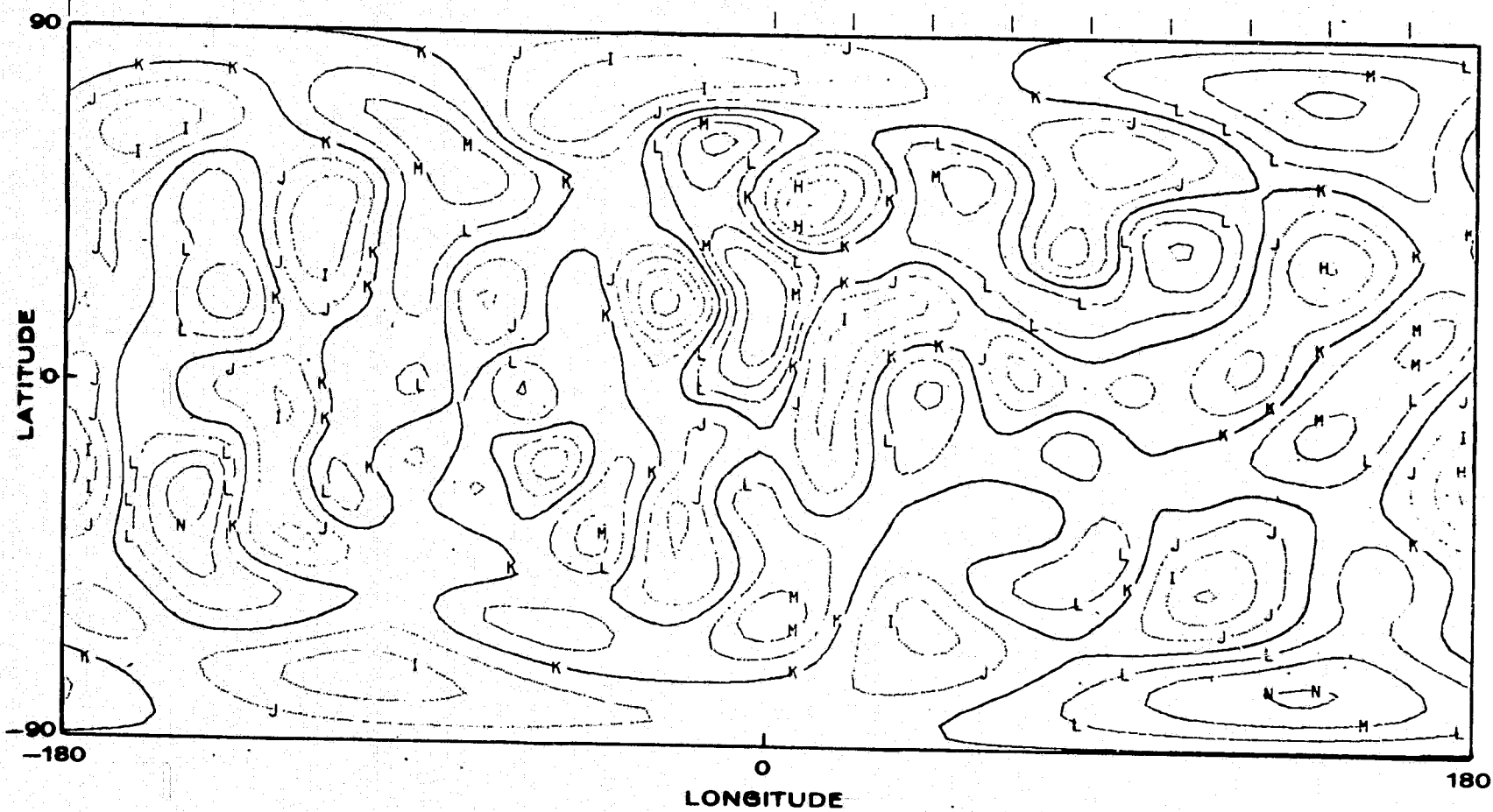
Table 4. Mass Locations and Values from SST (Continued)



Table 4. Mass Locations and Values from SST (Continued)

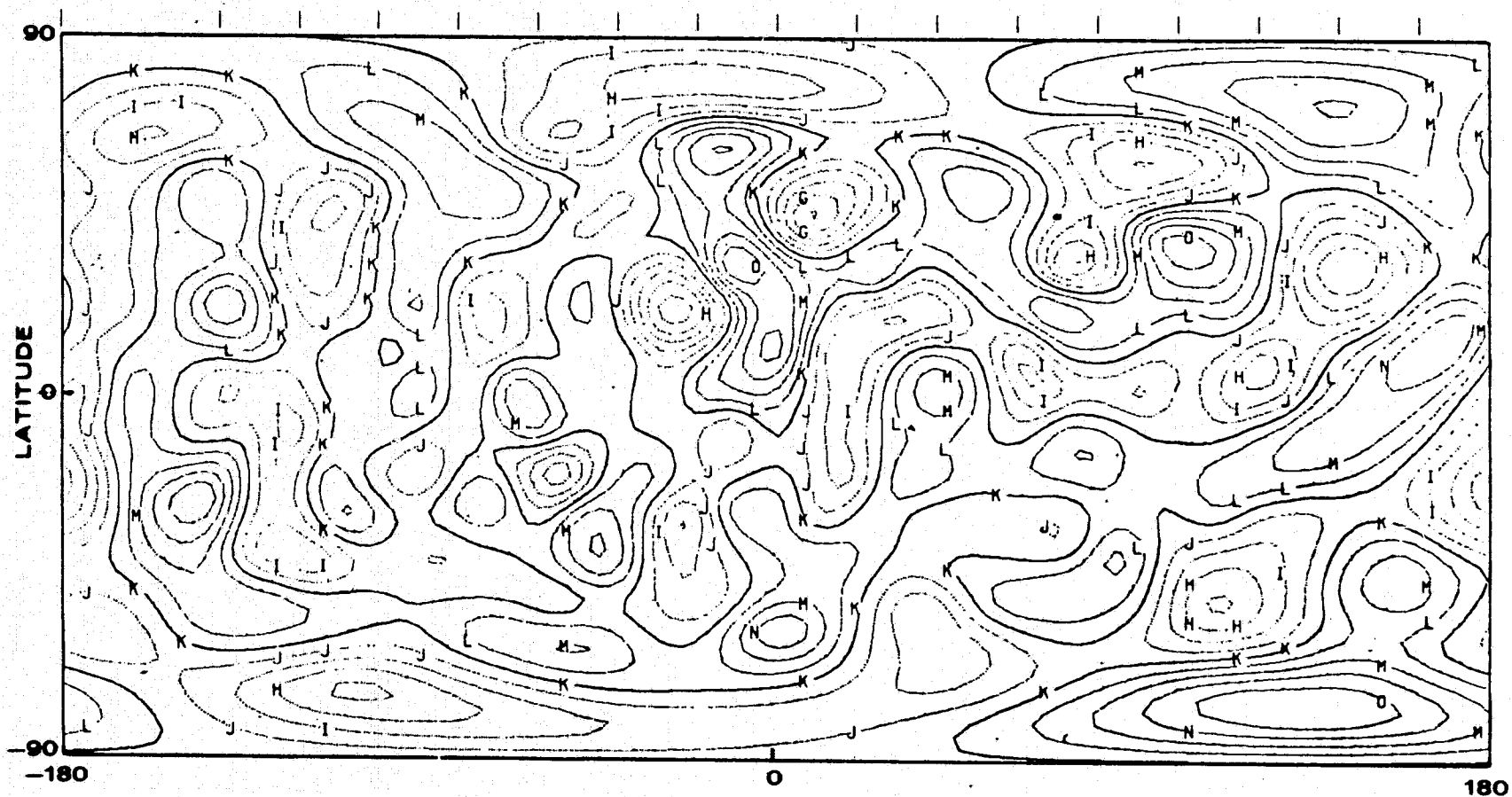
LAT	LONG	MASS									
313	42.0	64.8	.3162E-08	331	52.6	0.0	.2955E-07	349	61.9	-13.3	-.1322E-06
314	42.0	136.8	.2428E-07	332	52.6	72.0	.1066E-07	350	68.9	36.0	-.2591E-07
315	42.0	-151.2	-.2449E-17	333	52.6	144.0	.4978E-08	351	68.9	108.0	-.2508E-07
316	42.0	-76.2	-.1627E-07	334	52.6	-144.0	-.4967E-07	352	68.9	180.0	.1487E-08
317	42.0	-7.2	-.2578E-07	335	52.6	-72.0	-.5733E-07	353	68.9	-108.0	-.5257E-07
318	47.7	36.0	-.5009E-08	336	58.3	36.0	-.5473E-07	354	72.6	72.0	-.1978E-07
319	47.7	108.0	-.1765E-08	337	58.3	180.0	.2404E-07	355	72.6	-144.0	.3731E-07
320	47.7	-108.0	.7220E-07	338	58.3	-108.0	-.2337E-08	356	72.6	-72.0	.7722E-08
321	47.7	-36.0	.3616E-07	339	58.3	-36.0	-.1704E-07	357	72.6	0.0	.4984E-07
322	51.6	-138.0	.1385E-08	340	61.9	13.3	-.9913E-08	358	79.4	108.0	-.3089E-07
323	51.6	-163.0	.2975E-07	341	61.9	85.3	.5978E-07	359	79.4	180.0	-.1141E-07
324	51.6	-61.0	-.1882E-07	342	61.9	157.3	-.3108E-07	360	79.4	-108.0	-.3353E-07
325	51.6	-161.0	-.3193E-17	343	61.9	-130.7	.1558E-07	361	79.4	-36.0	.4034E-07
326	54.6	-9.0	.7063E-07	344	61.9	-58.7	.9384E-07	362	90.0	0.0	.1412E-07
327	54.6	61.0	.4468E-07	345	61.9	58.7	.2572E-07				
328	54.6	130.0	-.3132E-07	346	61.9	130.7	-.3706E-07				
329	51.6	-138.0	-.3288E-08	347	61.9	-137.3	-.7769E-07				
330	51.6	-163.0	-.2363E-07	348	61.9	-85.3	-.6152E-07				





K = 0; each level equals 0.4 milligals, L = .4, M = .8, etc.

Figure 6. Mass Layer Vertical Acceleration at 850 km Altitude ( $\sigma_a = .3 \times 10^{-7}$  earth)



K = 0; each level equals 0.4 milligals, L = .4, M = .8, etc.

Figure 7. Mass Layer Vertical Acceleration at 850 km Altitude ( $\sigma_a = .5 \times 10^{-7}$  earth)

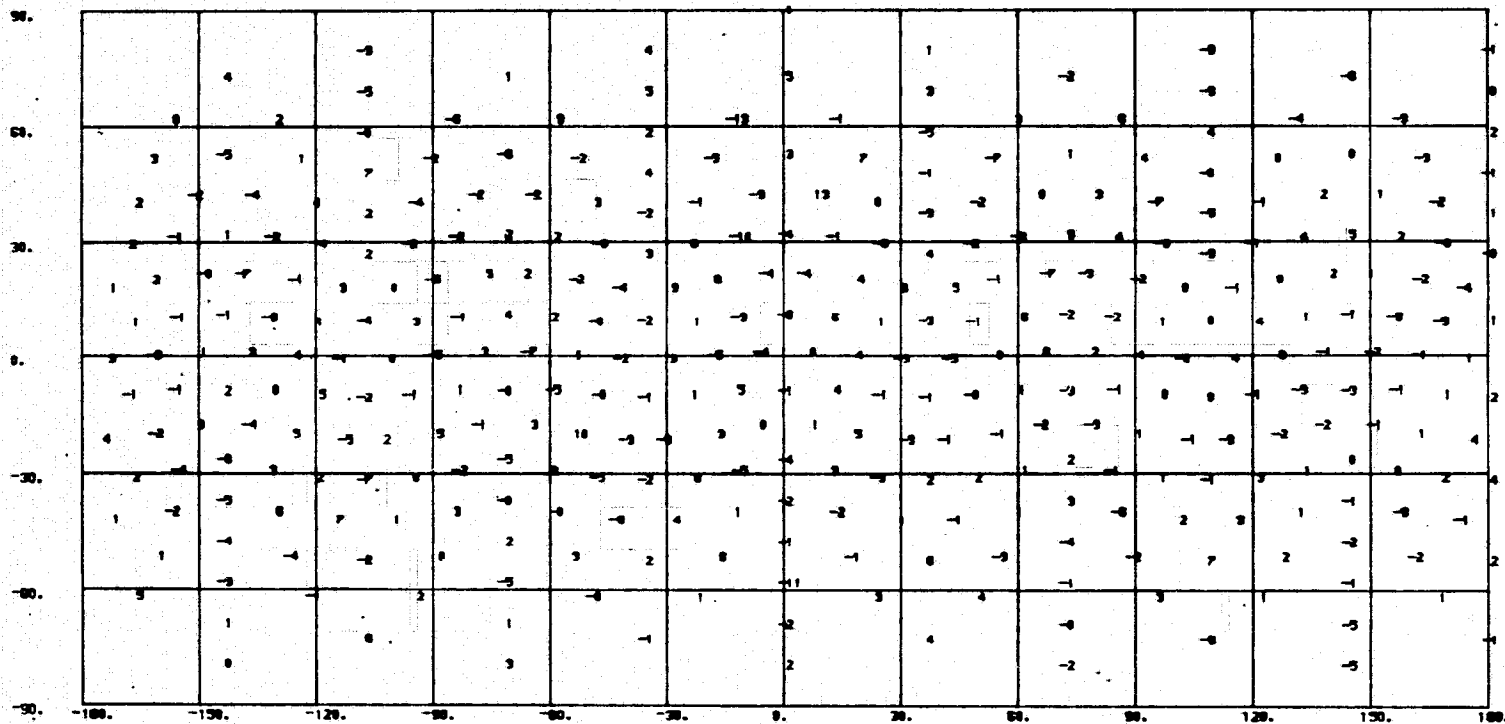
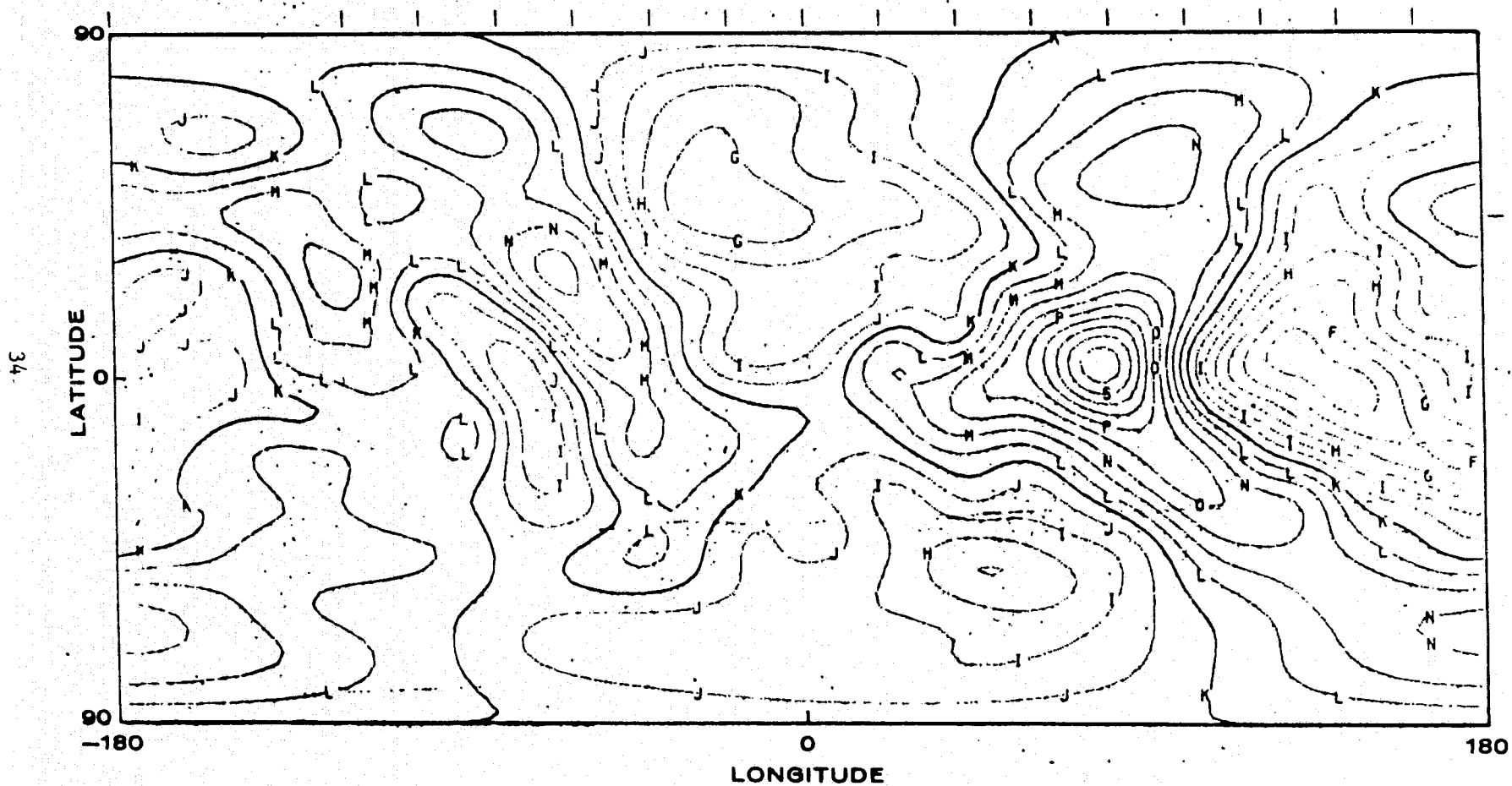


Figure 8. Geographic Distribution of Mass Anomalies

REPRODUCIBILITY OF THE  
ORIGINAL PAGE IS POOR



K = 0; Each level = 4 milligals, L = 4, M = 8, etc.

Figure 9. Total Vertical Acceleration Sensed by GEOS (GEM-6 plus mass layer)

Also we did not include a Brun's term. The same convention was used in plotting both Figs. 6 and 7. The positive contours correspond to regions of mass deficiency or negative surface anomaly. Some significant features of the acceleration map are:

Negative Accelerations (Positive gravity and mass anomalies)

Latitude	Longitude	Acceleration	~ Total Mass in Vicinity
10	20	-1.2	$1.6 \times 10^{-7}$
46	9	-1.6	+2
21	-28	-1.6	2

Positive Acceleration (Negative gravity and mass anomalies)

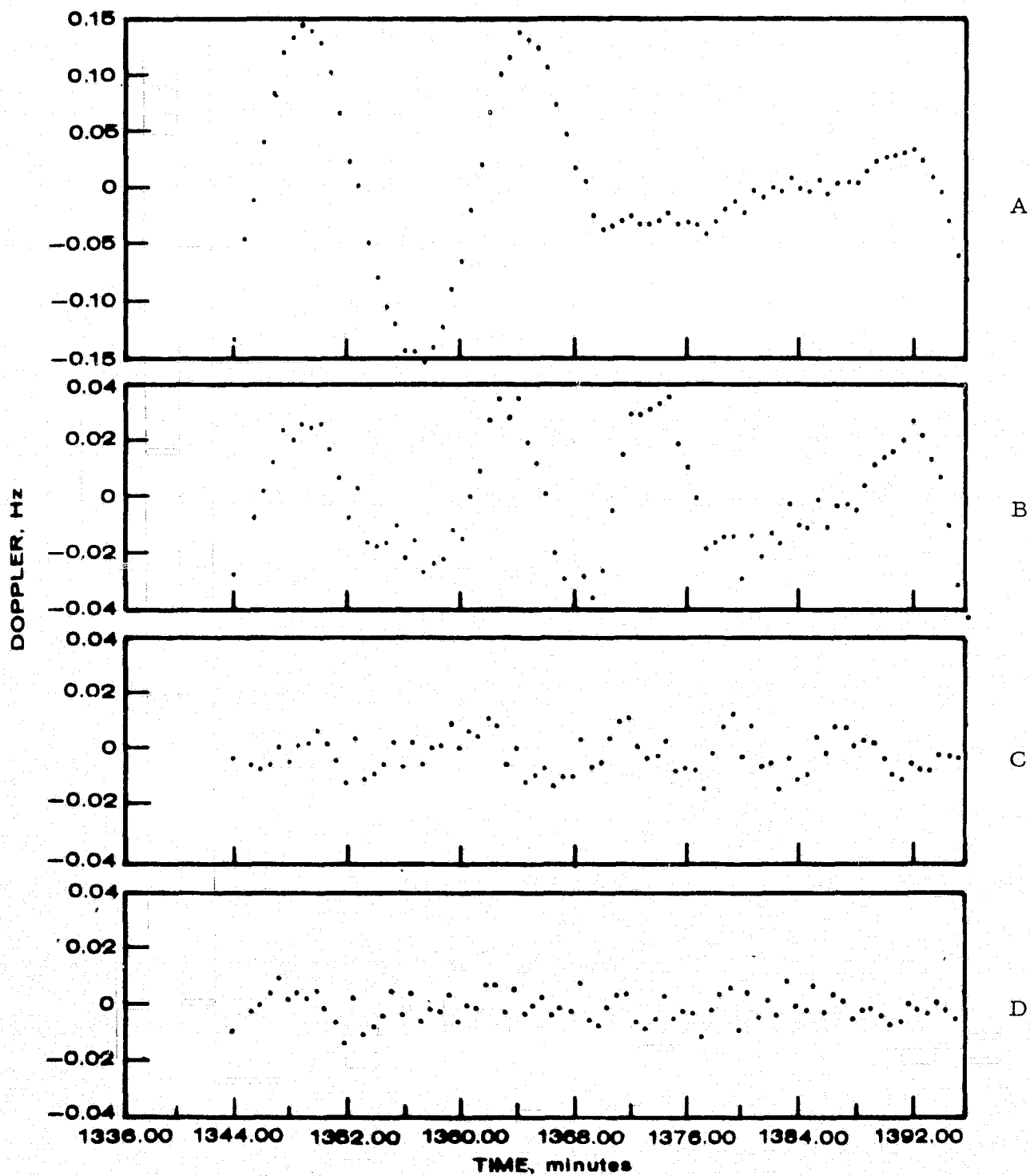
61	-15	1.2	-2
21	-2.5	1.2+	-3

## 2.10 Doppler Residuals

Some typical residuals before and after the fit are shown in Figs. 10 and 11, the latter improvement is less evident than the former. To show the effects of various levels of modeling, we also included residuals relative to a 2,0 earth model, GEM-6 truncated at the 6<sup>th</sup> degree, full GEM-6, and GEM-6 plus mass layer all for rev 268. Evidently, improvements are difficult to come by after GEM-6. The RMS levels were:

<u>Model</u>	<u>RMS Doppler Residual</u>
Principal oblateness only (2, 0)	.075 Hz
GEM-6 terms to 6-6 only	.020
GEM-6 complete	.0070
GEM-6 plus mass layer	.0055

Figure 12 shows residuals of a pass not included in the least squares solution. It can be seen that the improvement (RMS = .008 for GEM-6 vs .0057 for GEM-6 plus mass layer) is on the same order as the passes illustrated above.



A.  $C_{20}$ ,  $C_{40}$  only RMS = .075 hz; B. GEM-6 through degree 6 RMS = .02 hz;  
 C. Full GEM-6, RMS = .007 hz; D. GEM-6 plus mass layer, RMS = .0055 hz.

Figure 10. Doppler Residuals for Rev 268

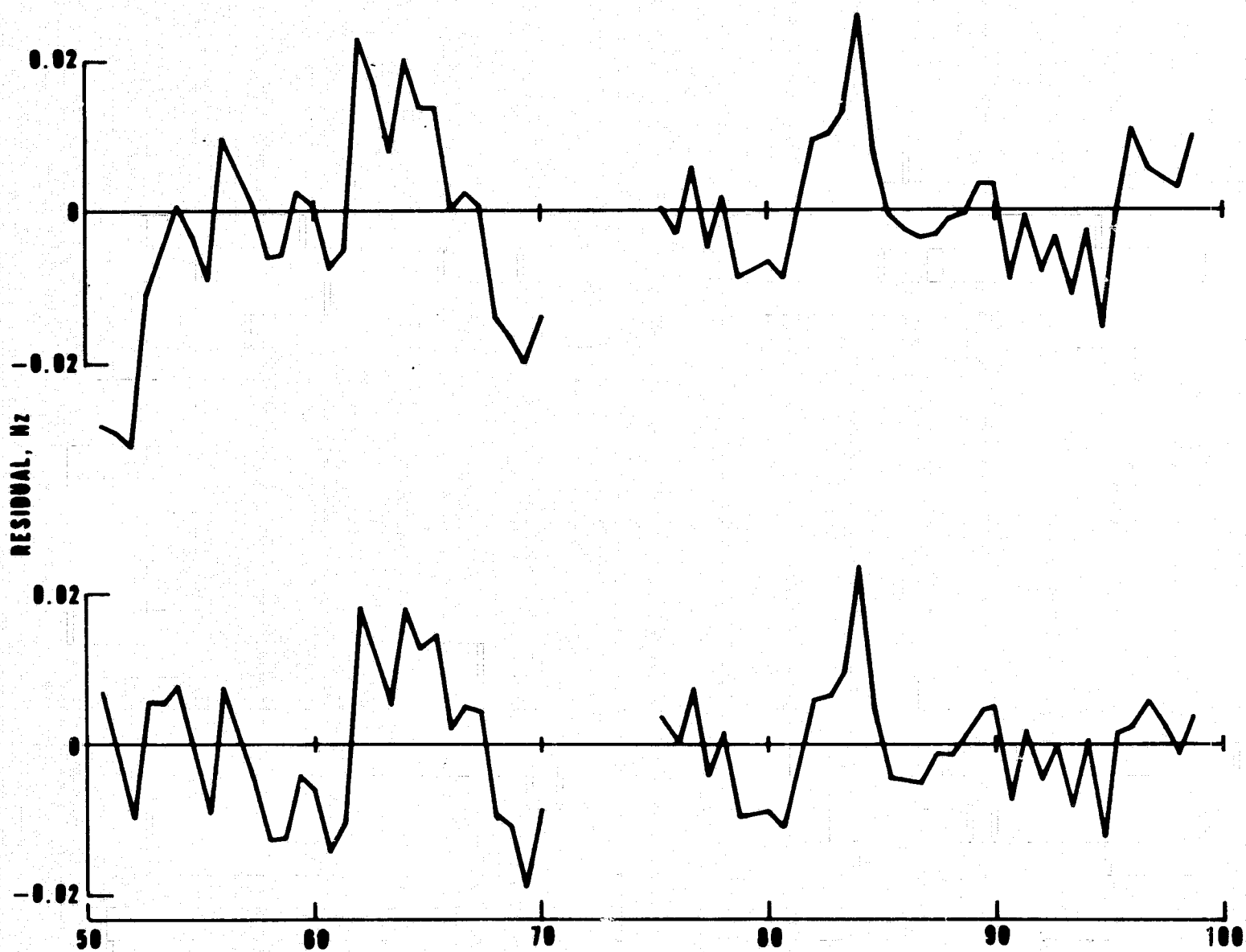


Figure 11. Doppler Residuals for Rev 925

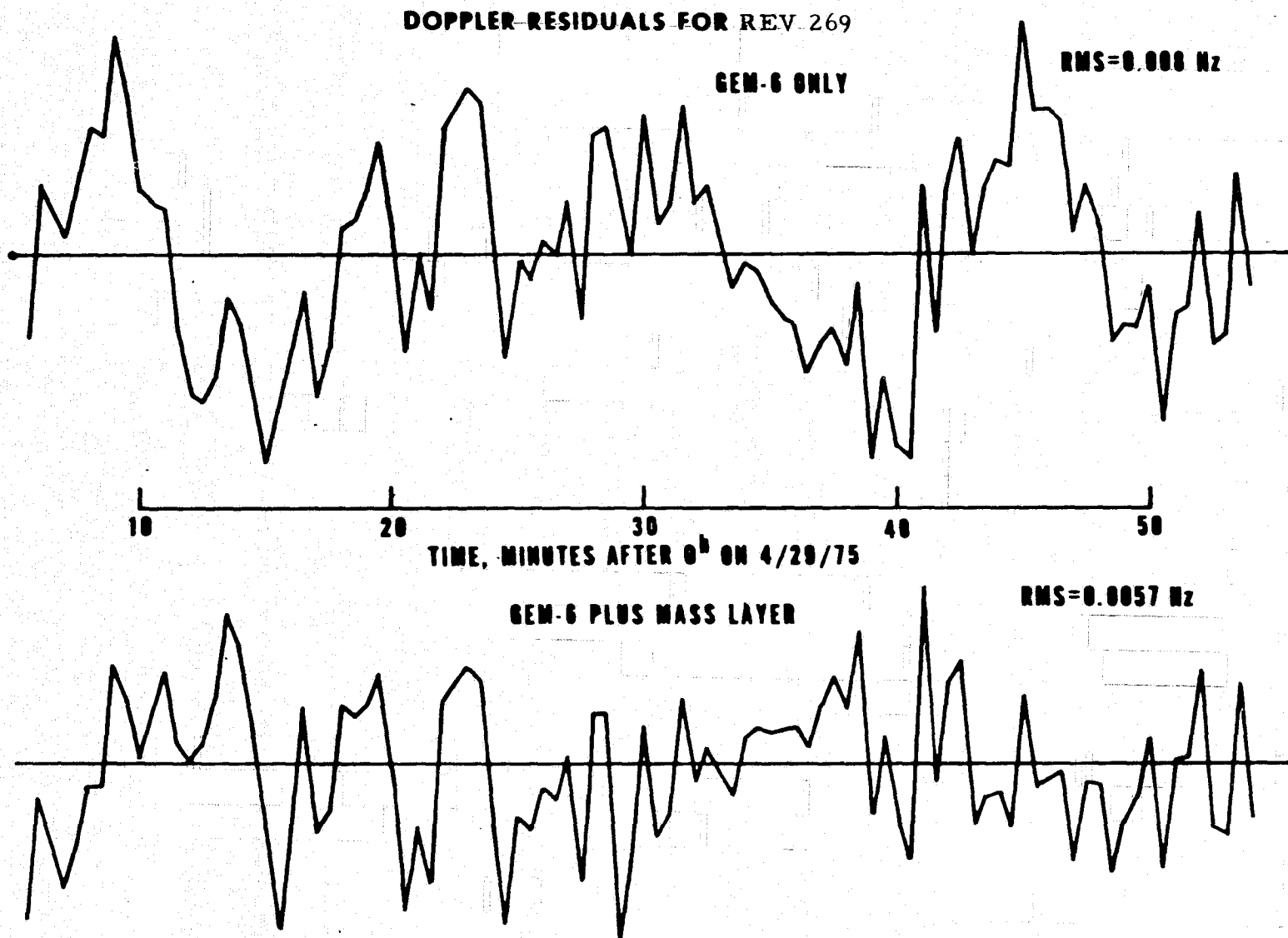


Figure 12. Doppler Residuals for Rev 269



The very low level of signature to begin with coupled with the excellent starting states and the highly linear nature of the method enabled us to obtain convergence in a single iteration. This was evident in evaluating residuals after the solution. We therefore did not reevaluate the partials for further iterations.

## 2.11 Conclusions and Discussions

The principal conclusions from our study of the SST data are:

- SST tracking is a viable technique to measure the earth's near field. Excellent coverage can be obtained from just a few stations with little or no tracking gaps.
- At GEOS-C altitude, the residual accelerations relative to GEM-6 are on the order of 1-2 milligals. With a measurement noise of .0055 - .007 Hz observed on many of the doppler passes, the accuracy of the short arc method of inference is about .3 to .5 milligals over the regions with reasonably good coverage.
- The advantages of the short arc dynamical method are: high degree of linearity, short integration time, little aliasing due to plant noise, and adaptability to incomplete data coverage. The method is a reasonable approach for the analysis of SST data for the recovery of gravity disturbances at altitude.
- Principal deficiencies in the current solution are:
  - a. Degraded geometry for many of the passes, high sensitivity passes with small GEOS to ATS angles account for only 75 percent of the data. Even for the ones with good geometry, sensitivity at the beginning and end are reduced.
  - b. Much of the earth's surface is not covered by good SST passes.
  - c. The GEOS orbit altitude is excessively high to sense some of the shorter wavelength terms.
  - d. Many good geometry passes contained dropouts or noise bursts at small GEOS to ATS angles. Even the nominal noise level is too high to sense the residuals relative to GEM-6. An improvement by a factor of 2 or 5 would be highly desirable.

## 2.12 Recommendation

As a project for the future, we would suggest the following experiment to map the remaining earth field. Launch a low altitude, polar satellite with perigee / apogee altitude of approximately 200/1000 km and track it with SST doppler from a high altitude polar satellite. The advantage of such a configuration is that both poles as well as the equatorial zones will be completely covered by passes with near ideal geometry. All of the non-hardware related deficiencies in the present data can be removed. All intermediate altitudes can be sampled as the argument of perigee precesses.

### III. Altimeter Analysis

The objectives of the analysis are: 1) derive smoothed estimates of geoid height from multiple passes over a given area, 2) obtain a representation of the geoid by a set of source parameters more compact than the original data set. These sources can be used to extrapolate the geoid to local areas not actually covered by measurements, and 3) infer gravity anomalies from the altimetry by virtue of the causal relations between geopotential, mass, and gravity.

In view of the very extensive amounts of altimetry from GEOS, our scope is necessarily limited. We were designated as one of the investigators to analyze data over the Atlantic Test Area. Our initial plan was to independently determine GEOS ephemeris from C-band laser and other ground tracking but it became apparent very quickly that the available resources do not permit such a course.

It was our intent to separate the geoid undulations into low and high degree components in the same manner as the SST analysis of Section II. The motivation here was the same as before--to see what part of the geoid was represented by the low degree harmonics and determine the spacing of a density layer for representing the remainder. Once again GEM-6 served as the base harmonic model.

An outline of our tasks, then, is as follows:

- (1) Select data base from altimeter tapes
- (2) Edit data to remove outliers and land mass reflections
- (3) Apply tide and known bias corrections
- (4) Make crossover adjustment on heights
- (5) Establish grid of representation elements
- (6) Calculate geoid residuals relative to GEM-6
- (7) Infer source magnitudes from geoid residuals of step 6
- (8) Calculate gravity anomalies from inferred sources and compare with observations

### 3.1 Data Base

The original data base consisted of 14 CALTOR BCD tapes containing approximately 150 passes. An initial screening chose passes contained within the quadrilateral shown in Figure 13. The figure is approximately equivalent to the Mission Plan test area in size with some displacements in the vertices. All points interior to the quad were accepted and the remainder rejected. The reason for displacing the vertices was to choose sides which were very nearly parallel to GEOS passes so that each one would be essentially complete except for possible truncation at the end thus assuring the maximum number of orbit crossovers. From the 140 original passes, 82 were initially selected with approximately 7000 observations. These had to be edited for outliers and land mass reflections of which there were a considerable number, because the southwest edge of the quad contained many islands. Table 5 lists the passes actually used in the analysis. The final base contained 74 passes with ~6050 data points at approximately 3 second intervals.

### 3.2 Crossing Adjust

After the edit, the next task was to adjust the height of the passes for possible biases and satellite radius errors. The adjustment was made in a least squares sense by minimizing the quadratic sum of the geoid height differences at the crossover points, i. e., we find corrections,  $\delta R_i$ ,  $\delta R_j$  which minimize S where

$$S = \sum_{j>i}^m (N_i - N_j + \delta R_i - \delta R_j)^2 \quad m = \text{number of crossovers}$$

$N_i$ ,  $N_j$  are the geoid heights (sea height less tide) at the crossing of the  $i^{\text{th}}$  and  $j^{\text{th}}$  arc. An a priori reciprocal variance of  $\sigma^2 = 100 \text{ m}^2$  was added to the diagonal of the normal equations to stabilize the solution. The adjustment should converge in one iteration since the partial derivatives are constants equal to  $\pm 1$ . Actually we made two iterations because passes were deleted after the first correction due to some rather large residual differences even after the biases were applied. Some statistics on the crossover adjusts are:

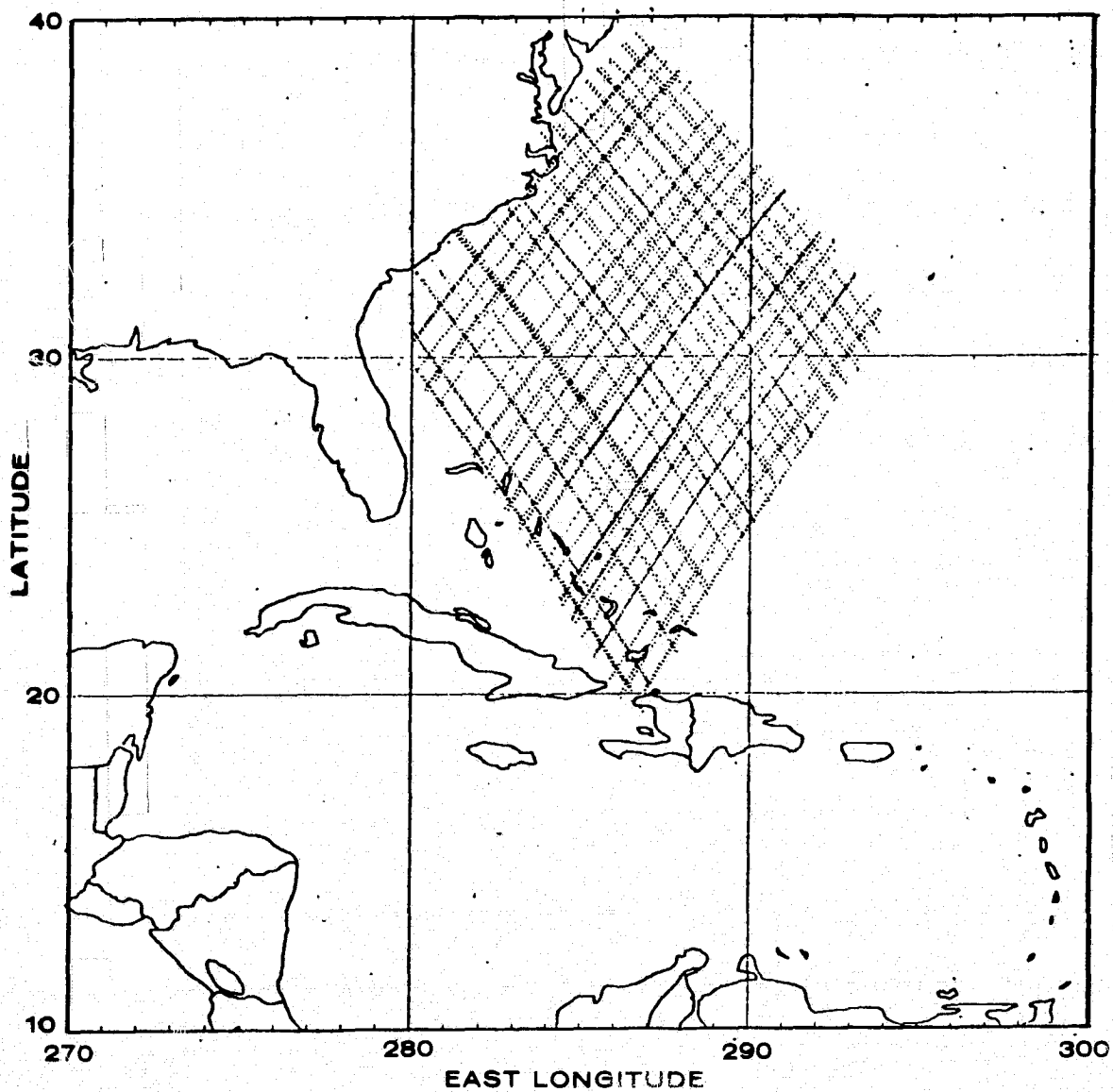


Figure 13. Earth Traces of Altimetry Passes

Table 5. Summary of Altimetry Passes

NP	REV	CAY	SEC	DT	BIAS	NPT	AD
1	189	113	290	177	-2.68	55	A
2	246	117	315	205	-2.11	101	A
3	265	118	307	187	-1.63	77	A
4	402	128	333	176	-1.45	90	A
5	254	117	822	193	-1.41	55	A
6	203	114	282	94	-1.70	33	A
7	258	116	184	211	-0.80	90	A
8	329	122	339	199	-0.80	90	A
9	331	123	323	70	-0.17	22	A
10	333	123	831	217	-0.89	50	A
11	374	126	356	95	-0.80	30	A
12	843	159	487	184	-1.19	51	A
13	851	160	132	64	-0.47	20	A
14	857	160	478	194	-2.40	30	A
15	1107	173	212	196	-0.85	36	A
16	1156	173	563	107	-1.81	37	A
17	1509	206	327	176	-0.56	32	A
18	1511	206	675	186	-3.42	92	A
19	1582	211	691	182	-7.72	50	A
20	1590	212	333	219	-9.99	100	A
21	1647	216	359	269	-3.46	93	A
22	1696	219	740	195	-1.91	63	A
23	1875	233	443	194	-1.60	50	A
24	2031	227	432	193	-3.93	50	A
25	2037	233	330	188	-1.45	50	A
26	1738	227	765	213	-5.38	99	A
27	2094	247	855	182	-1.68	50	A
28	2102	248	496	158	-1.48	77	A
29	2168	248	394	182	-1.11	50	A
30	2144	252	525	186	-1.88	50	A
31	2159	253	511	207	-0.33	66	A
32	2244	258	531	213	-2.10	101	A
33	2300	127	380	180	-3.82	81	A
34	2387	141	405	166	-8.32	82	A
35	2372						
36	2350						
37	2358						
38	388						
39	197						
40	1263						
41	1789						
42	1846						
43	1440						
44	1710						
45	2506						
46	1960						
47	1965						
48	1974						
49	2017						
50	2068						
51	2770						
52	2890						
53	2898						
54	2933						
55	2941						
56	3069						
57	3097						
58	3154						
59	3260						
60	1298						
61	1653						
62	2696						
63	2756						
64	2150						
65	2307						
66	538						
67	837						
68	1178						
69	1227						
70	1568						
71	1599						
72	1766						
73	1766						
74	1766						
75	1766						
76	1766						
77	1766						
78	1766						
79	1766						
80	1766						
81	1766						
82	1766						
83	1766						
84	1766						
85	1766						
86	1766						
87	1766						
88	1766						
89	1766						
90	1766						
91	1766						
92	1766						
93	1766						
94	1766						
95	1766						
96	1766						
97	1766						
98	1766						
99	1766						
100	1766						

NP = pass number; All passes in 1975 except 73, 74 which are in 1976; DT = duration of pass; BIAS = best estimate of bias from crossing adjust; NPT = number of observations; AD, A = ascending, D = descending.

### Crossing Adjust Statistics

	<u>Case 1</u>	<u>Case 2</u>
Number of Passes	82	74
Number of Intersects	1448	1148
<u>RMS Height Difference</u> - meters		
Before	16.0	1.28
After	1.37	.92
RMS <u>Bias</u> - meters	11.26	6.04 (3.3)
Mean Bias - meters	.031	.28

The corrections obtained from the second case were added to the observed heights to obtain the corrected geoid. If five of the final 74 biases with magnitudes greater than 10 meters were excluded, the RMS bias was reduced to about 3.3 meters. The probable accuracy of the ephemeris radius is then  $3.3/\sqrt{2} \approx 2.3$  meters. One bias which cannot be removed by the preceding is the absolute or constant calibration bias [11]. That one was taken out just prior to the mass layer regression.

Before proceeding to the next steps of the analysis, we make a digression on the problem of representation.

### 3.3 Representation

Some candidate elements of representation are:

(N = geoid height, g = gravity anomaly, m = mass element)

- (1)  $N \rightarrow \Delta g$  Molodenskii 1962 [12]
- (2)  $N \rightarrow m$  Chovitz [13]
- (3)  $\Delta g \rightarrow N$  Stokes' formula Heiskanen, Moritz [14]
- (4)  $m \rightarrow N$  Classical potential
- (5)  $N \rightarrow f(\phi, \lambda)$  Polynomial expansions in latitude ( $\phi$ ) and longitude ( $\lambda$ )

The first two express the sources as a convolution of the measured height and an influence or kernel function over a sphere. They require observation data over the entire surface. Since this is generally not available, the currently popular approach is to use observations near the point of interest and substitute geoid values from a spherical harmonic expansion outside of an assigned polar angle limit. The same requirement exists for methods 3 and 4. Our main interest is centered on method 4. The others are being pursued by other investigators.

There is considerable similarity between Stokes' formula and the classical potential

$$N = \frac{1}{4\pi\gamma a} \int_{\sigma} S(\psi) \Delta g(\psi) d\sigma \quad \text{Stokes}$$

$$N = a^2 \int_{\sigma} \frac{dm}{\rho} = a^2 \int_{\sigma} \frac{\chi(\psi) d\sigma}{\rho} \quad \text{Classical Potential}$$

where  $S(\psi)$  is Stokes' kernel,  $\gamma$  and  $a$  are mean gravity and earth radius, respectively;  $d\sigma$  is an element of area on the surface  $\sigma$ ,  $\rho$  is the distance from the source to the field point;  $\chi(\psi)$  is an equivalent surface density,  $dm$  is an element of mass (in units of earth mass). The representation elements are  $\Delta g, d\sigma$  and  $\chi d\sigma$ , respectively. Hence, the difference in the two equations is a matter of the difference between Stokes' and the  $1/\rho$  kernel. Assuming that the density elements are located on the surface of a sphere and letting  $t = \sin \frac{\psi}{2}$ , then

$$\frac{2a}{\rho} = \frac{1}{t}$$

$$S(\psi) = \frac{1}{t} - 6t + 1 - 5 \cos \psi - 3 \cos \psi \ln(t + t^2)$$

For small values of  $\psi$ , both kernels have a  $1/t$  type singularity;  $\frac{a}{\rho}$  has an extra factor of 2 in the denominator\*. Figure 14 shows the two functions for  $\phi \geq 10^\circ$ .

---

\*The extra factor of  $1/2$  is immaterial since it cancels out in the ratio  $\rho(\psi)/\rho(\psi < 10^\circ)$ . This ratio is indicative of how rapidly the integral converges with  $\psi$ . Hence, it is simpler to compare Stokes' with  $\csc \psi/2$  rather than  $(1/2) \csc \psi/2$ .



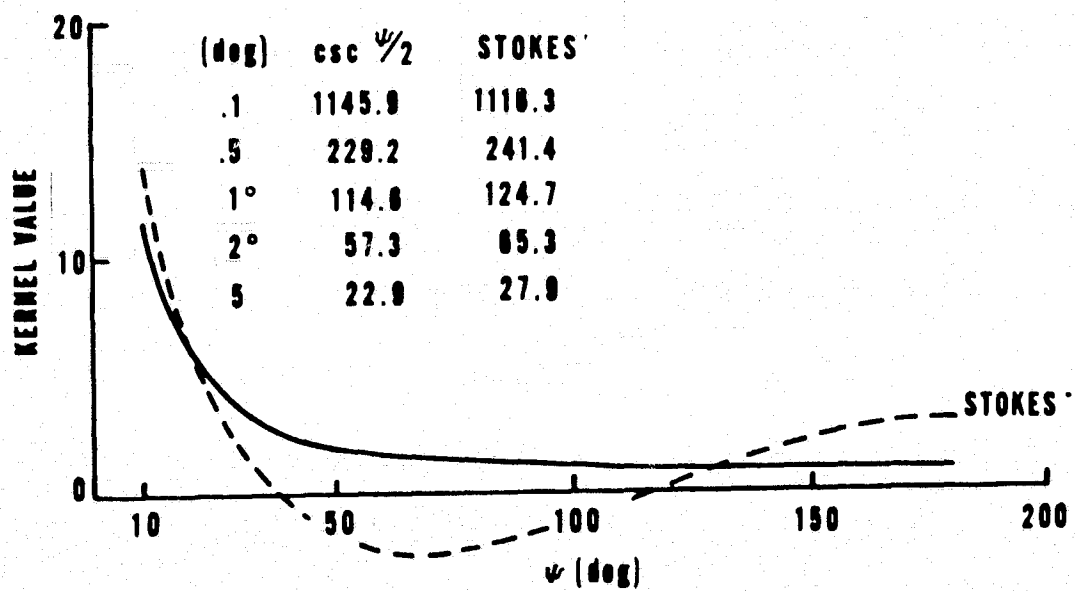


Figure 14. Stokes' and Inverse Distance Kernel

Magnitudewise, Stokes' kernel is larger over most of the range but it passes through zero at two points with two sign changes. The fact that the  $1/\rho$  kernel has the same sign is of little consequence since the source elements are certain to change signs many times. On the other hand, the rapidity of the magnitude decay dictates the rate of convergence with increasing  $\psi$ . For practical purposes, the two representations are essentially equivalent since the kernels behave similarly near the origin and converge at approximately equal rates.

Equating the two expressions for  $N$  and retaining only the critical region near  $\psi = 0$ , one obtains:

$$\frac{1}{4\pi\gamma a} \int \Delta g \, d\sigma = a^2 \chi \frac{d\sigma}{\rho} \quad \text{or} \quad \frac{\Delta g}{4\pi\gamma t} = \frac{a^2 \chi}{2t}$$

which is the result of applying Gauss' theorem  $\nabla \cdot (\Delta g) = 4\pi G M \chi$  to a large plate.

Since both kernels become singular as  $\psi \rightarrow 0$  even though the integrals are well behaved, some care is needed to average and weight the elements with small  $\psi$ . One simple way to circumvent the singularity is to remove the discrete elements from the surface. Another is the use of finite (or distributed) masses either at the surface or at depth. Both methods result in a smoother variation of the potential (or geoid) than surface sources and are likely to be better representations of the actual data.

While the finite distributions are intuitively more appealing than point sources, the computation of the potential, even for very simple shapes is much more complex. To get some feel for the differences between point and distributed masses, we calculated the potential of a buried disk at various depths and compared its potential with that of a corresponding point mass. The potential of the disk was obtained by numerical quadrature (see Appendix I for algorithm). Two cases were examined.

- a. Disk and point mass at the same depth but with different masses such that both induced a geoid perturbation of 1 meter at a point on the surface directly over the mass (i. e., on the axis of the disk).

- b. Total disk mass equals point mass but with the latter at a greater depth such that both induce perturbations of one meter at the surface point directly over the mass.

We considered depths of  $b$  and  $2b$  where  $b$  is the radius of the disk. For the sake of brevity, only the results of (a) will be shown since differences for (b) are smaller.

Figure 15a shows the geoid heights  $N_d$ ,  $N_p$  for the disk and point source, respectively, versus normalized distance from the axis  $\rho = r/b$ , and  $\zeta = Z/b$  with  $b = 20$  nmi where  $Z$  and  $r$  are coordinates along and perpendicular to the disk axis, respectively. The percent differences between the two are shown in Figure 15b. Significant differences exist mainly for small values of  $\zeta$ ,  $\rho$  as one expects. When these normalized variables exceed 2, the disk begins to resemble a point source. In the critical region of small  $\rho$ ,  $\zeta$ , the differences grow almost linearly from zero to the steady state values of  $\sim 18$  and 5 percent, respectively, with the disk having a slower decay rate.

The gravity anomaly and their differences shown in Figure 16 are another matter. The fall off of gravity for the point mass is significantly sharper than the disk. The combination of both observables, i. e., gravity and geoid (or potential) could eventually provide a basis for the choice of a model. Since the current altimetry data base completely overwhelms the amount of available gravity data, we decided to start with a point mass model because of its simplicity and rather mild geoid differences noted above. If and when the residual signatures in altimetry or gravity dictate a more refined model, software for computing the potential of the disk or even solids will be available.

Having chosen the point mass model, there is still the matter of a starting grid spacing and depth. Again, there is no hard or fast rule. We chose an initial spacing of 111 km (1 deg) and depths of 55.5 km and 111.1 km. Experiments will be the guide in dictating other choices.

### 3.4 Some Remarks on Representation

The basic problems in analyzing GEOS altimetry are representation and extrapolation to unmeasured points. The inference of gravity anomalies and disturbances is a related third problem. Given adequate coverage, the geoid

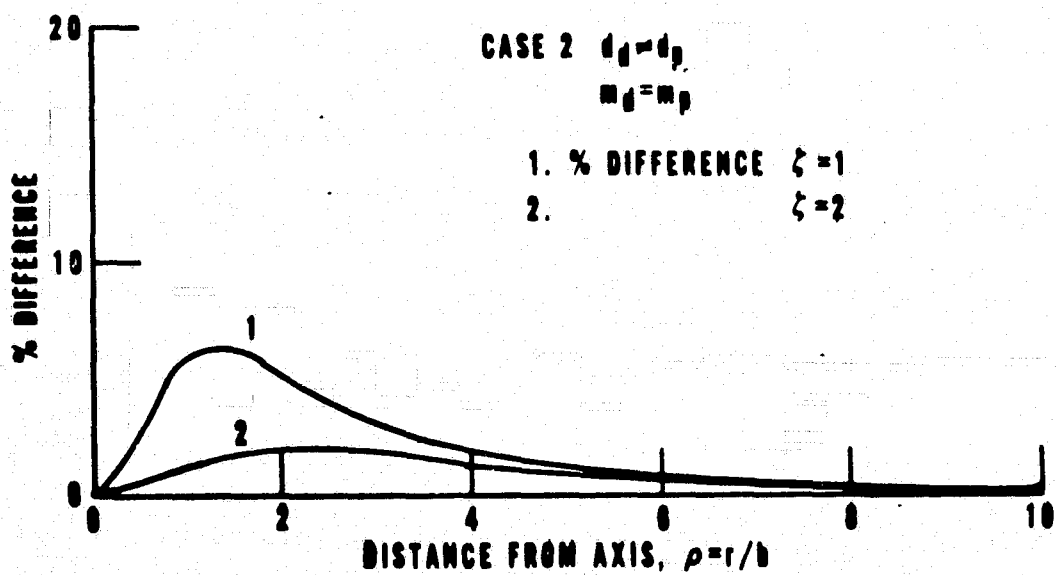
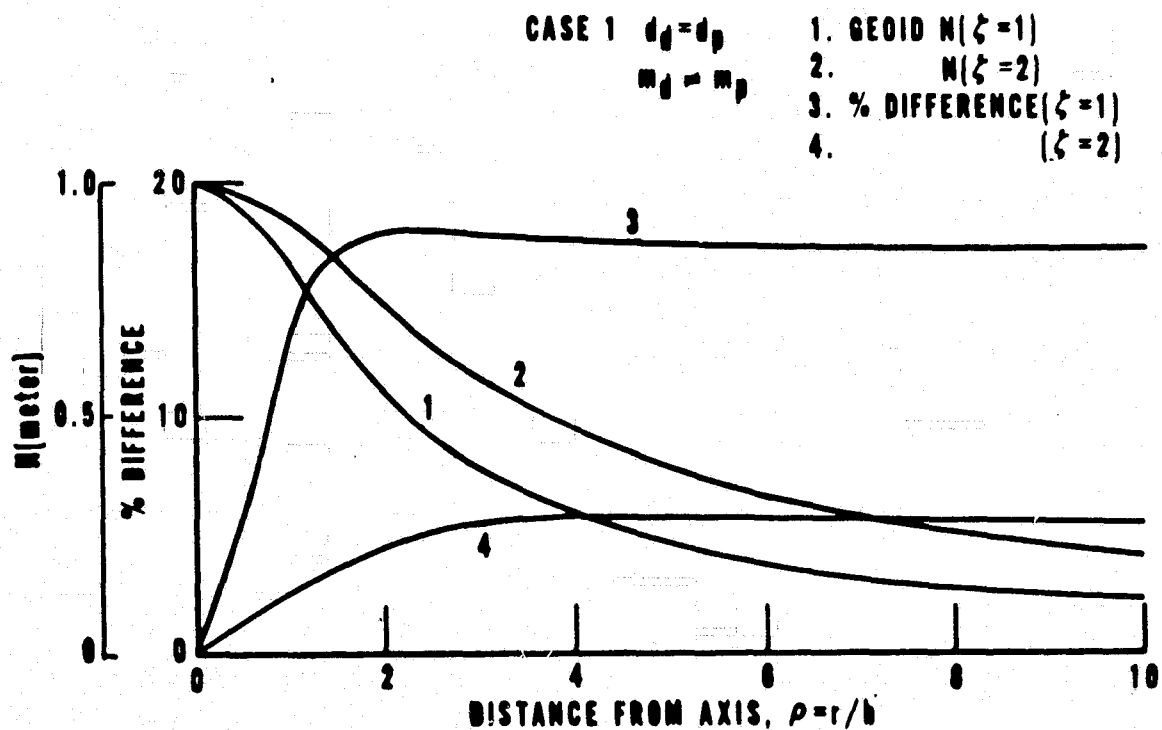


Figure 15. Geoid Difference Between Point and Disk Mass

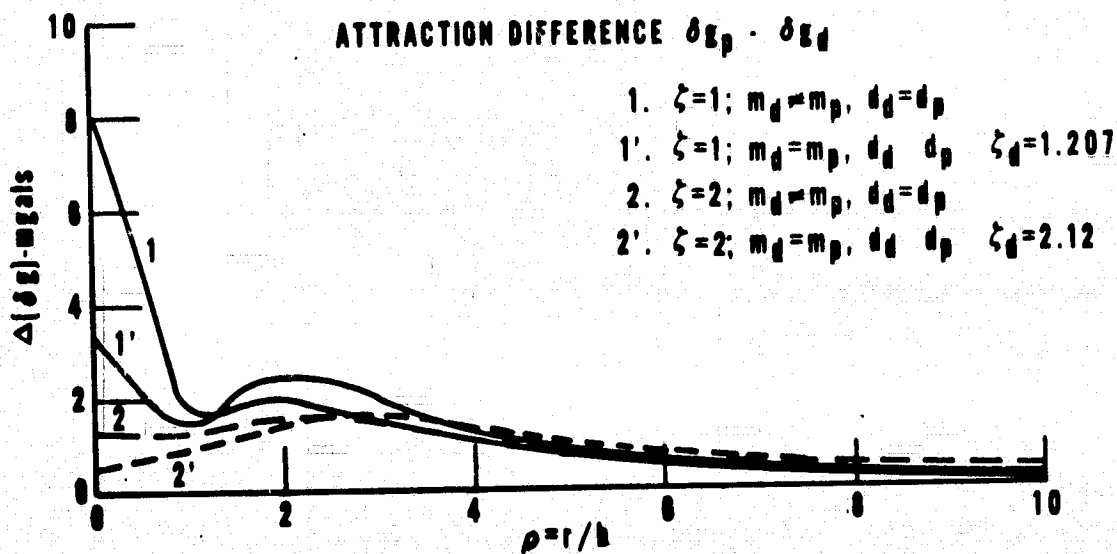
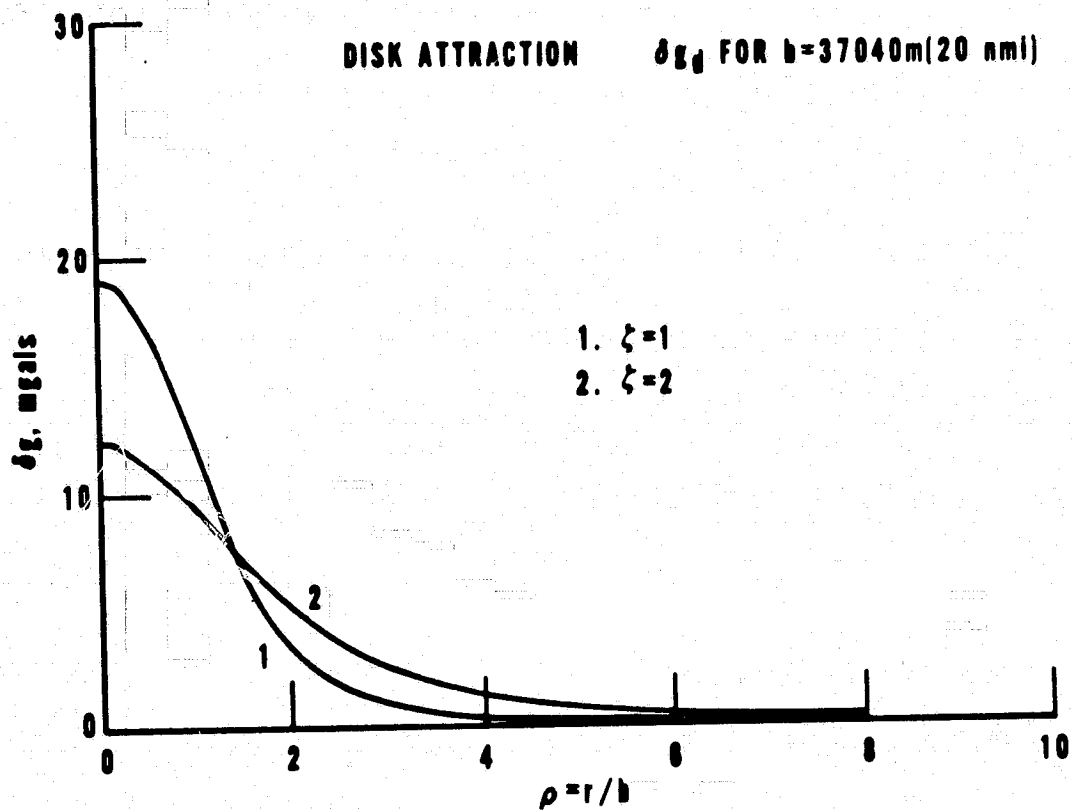


Figure 16. Gravity Disturbance Difference Between Point and Disk Mass

could be approximated locally by polynomials which can be splined to obtain any degree of continuity [15]. To be practical, the expansions must converge rapidly. The fitting functions are expected to be valid extrapolations of the geoid at unsampled points in the vicinity of the measurements because the potential is smoothly varying. (At least over distances on the order of a correlation length.) We also expect the derivatives of the fitting functions to be reasonable estimates of the vertical deflections and local gravity disturbances with errors which depend on the extent of the measured region.

Use of the fitting functions to extrapolate potential or gradient to another altitude is related to the third problem. Classical integral formulas allow such an extrapolation given coverage over a closed surface. In treating local areas, one justifies the extrapolation by noting that the kernels of the integrals fall off rapidly with distance and one can truncate the integration at some "small" distance within acceptable error limits. Physically, it is a matter of causality, local mass anomalies induce local disturbances.

Some desirable properties of the point mass kernel at depth are:

- (1) Function is harmonic and simple to compute
- (2) Can be fitted to match boundary conditions at surface
- (3) It is smoother than surface mass kernel with surface sources
- (4) Has the correct boundary condition at infinity
- (5) Has some physical significance
- (6) May be used to represent or infer gravity

### 3.5 Truncated Kernels

One aspect of the gravity anomaly to geoid ( $\Delta g \rightarrow N$ ) problem which has received some attention in recent years is that of missing measurements beyond some limiting angle  $\psi_{\max}$  away from the field point. In addition to the substitution of anomalies from harmonic models in the region  $\psi > \psi_{\max}$ , suggestions have been made to use a so-called "truncated" kernel to further lessen the error caused by incomplete data coverage. Stokes' kernel has been analyzed at some length in this respect. The idea is to remove the low degree

terms in the Legendre series expansion of the kernel and use orthogonality properties to show the improvements thus derived.

The same type of removal could be done in the case of the point mass kernel, i. e., in place of  $a/\rho$ , we used the kernel  $K_l$  where

$$K_l = \frac{a}{\rho} - \sum_0^l \left(\frac{a}{r}\right)^{n+1} P_n(\cos \psi)$$

Rather than go through the lengthy derivation of the error estimates, we graphically illustrate the functions  $K_l$ . The behavior of the  $K_l$  for  $l = 0, 4, 8, 12$  and  $2 < \psi < 65 \text{ deg}^*$  are shown in Figure 17. The more rapidly  $K_l$  decreases the faster the convergence with  $\psi$ . Using the point  $\psi \approx .27^\circ$  as reference where  $f(.27^\circ) = 100$ , the values of  $K_l$  for  $\psi > 2.5 \text{ deg}$  are all less than 15. In the region  $2.5 < \psi < 30 \text{ degrees}$ , the modified kernels are considerably smaller than the one with  $l = 0$ . Since all the  $K_l$ 's through  $l = 12$  are within 12 percent of  $K_0$  for  $\psi < .27^\circ$ , the more rapid decrease from about 2.5 to 30 degrees implies less error arising from loss of data within this zone.

### 3.6 Mass Layer Regression

A uniform grid with spacing of one degree between points was located beneath the quadrilateral in Figure 13. Inference of mass magnitudes at these points follows the usual weighted least squares algorithm. A single iteration suffices in each case because of the small residual amplitude relative to GEM-6. No a priori was added to the diagonals because of good data quality but the boundary points might have benefited from some degree of stabilization. Two mass depths were considered -- -55.5 km and -111.1 km.

The computed geoid height from GEM-6 followed Rapp's algorithm [16] with flattening  $f = 1/298.255$ . The  $C_{20}^*$  term was essentially zero while  $C_{40}^*$  was altered from the GEM-6 value of  $.536 \times 10^{-6}$  to  $-.254 \times 10^{-6}$  resulting in a geoid shift of about -4.25 meters over the quad.

---

\*  $a = (6378. - 55.5) \text{ km}$ ,  $r = 6378 \text{ km}$ , i. e., masses at 55.5 km depth.

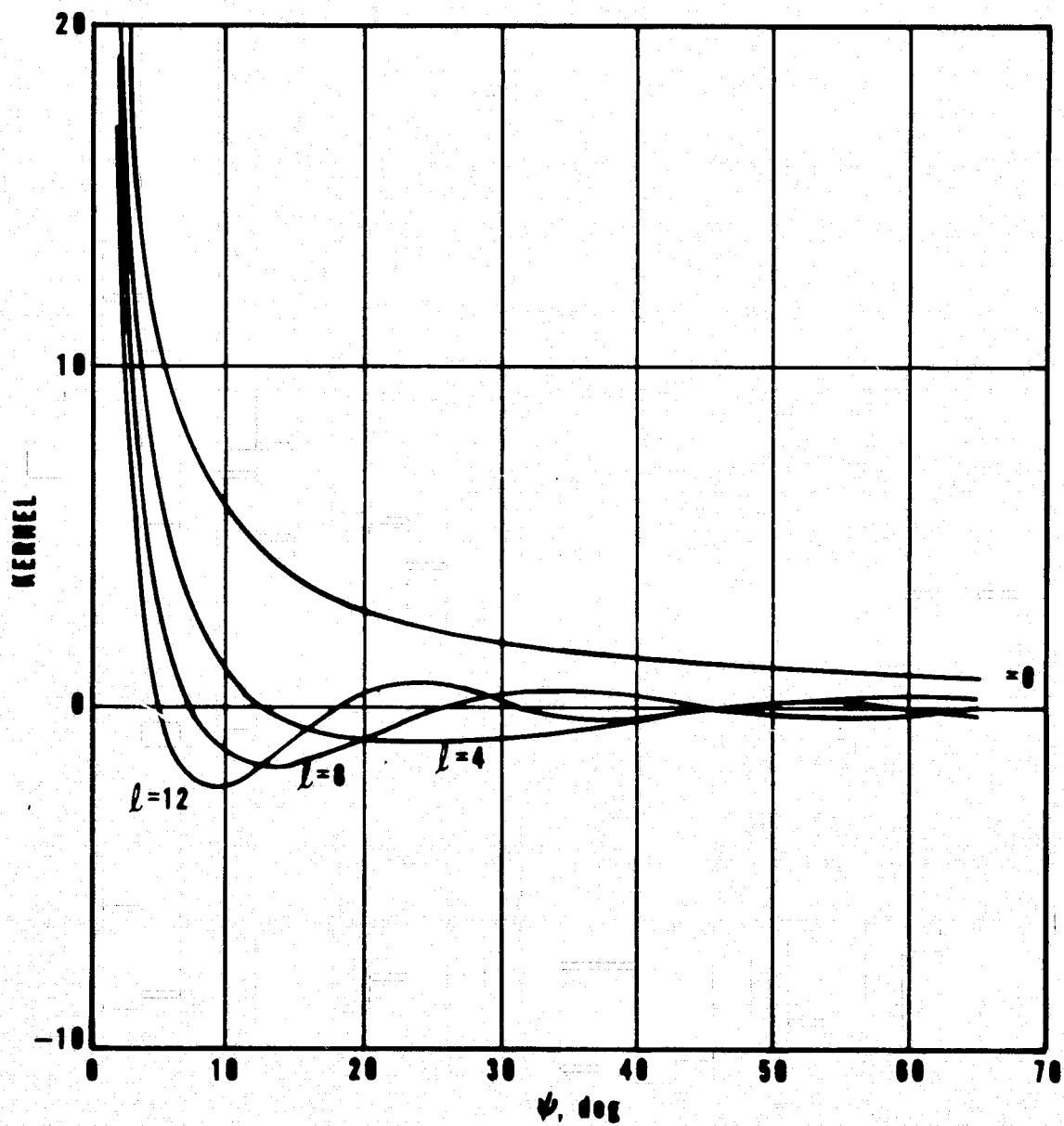


Figure 17. Modified Point Mass Geoid Kernel vs  $\psi$



**Table 6.. Mass Solution from Altimetry, Depth = -55.5 km**

[illegible]

### 3.7 Results

The smoothed geoid contours due to the mass layer over the test region are shown in Figure 18 and the inferred mass distribution in units of  $10^{-9}$  earth mass at depth -55.5 km are shown in Figure 19. Some statistics for the best solution (listed in Table VI) and several related ones are given in Table VII.

Table 7. Statistics of Mass Layer Solutions

	$C_{40}^* = 0.536 \times 10^{-6}$		$C_{40}^* = -0.254 \times 10^{-6}$	
	<u>No Bias</u>	<u>With Bias*</u>	<u>No Bias</u>	<u>With Bias*</u>
Mean residuals GEM-6 only (m)	1.556	5.106	-2.691	.858
RMS residuals GEM-6 only (m)	2.967	5.697	4.293	3.453
Mean residual (with masses) (m)		-.017	-.018	-.017
RMS residual (with masses) (m)		.717	.707	.711
Mean mass ( $10^{-9}$ earth mass)		.544	-.116	.196
RMS mass ( $10^{-9}$ earth mass)		4.458	4.218	4.330

The smallest mean geoid residual (without the mass layer) is obtained for the case  $C_{40}^* = -0.254 \times 10^{-6}$ . Calibration-bias-corrected residuals for this case, with and without the mass layer, are shown in Figures 20a and 20b, respectively. Many of the preadjust residuals are in the 6- to 7-meter range. Figure 20b indicates that the noise level of the data is even better than the RMS of 0.71 meters because there are still clearly discernable trends. Some of these may be due to ephemeris errors. It appears that the one-degree spaced grid is adequately dense for most of the regions. We have not attempted to insert more masses, even though some densification is evidently called for in some areas.

Since each observation was weighted by the inverse standard deviation, the mass estimates are also minimum variance. The formal standard deviation of each mass ranged from about  $3 \times 10^{-9}$  earth mass at the edges to  $0.3 \times 10^{-9}$  earth mass near the center. Truncation effects have not been included and would increase the uncertainty much more, particularly near the boundaries.

---

\*Calibration bias = -3.55 meters.

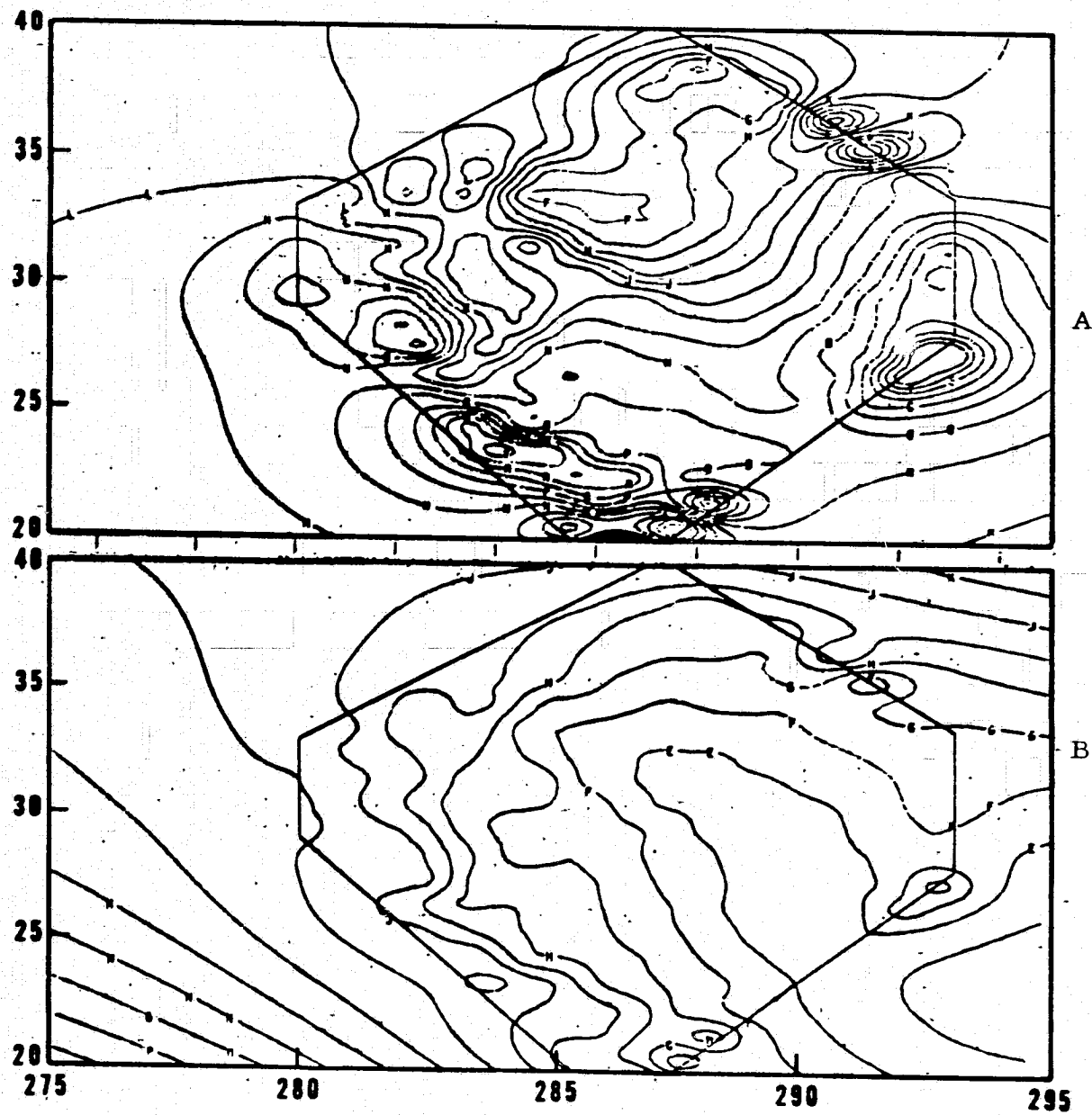


Fig 8A,  $K = 0$ , each level equals 1 meter,  $L = 1$ ,  $M = 2$ , etc.  
 Fig 8B,  $U = 0$ , each level equals 3 meters,  $T = -3$ ,  $S = -6$ , etc.

Figure 18. Geoid Heights from Mass Layer, Total Geoid

REPRODUCIBILITY OF THE  
 ORIGINAL PAGE IS POOR

## 58

40.						1				
38.					1	-4	7			
36.					1	-6	-4	1	-6	
34.					1	-1	-1	-4	-5	13
32.					2	2	-2	-1	-1	3
30.					-4	7	-4	X	0	-2
28.								1	-4	2
26.										3
24.										
22.										
20.										
18.										
16.										
14.										
12.										
10.										
8.										
6.										
4.										
2.										
0.										
	276.	278.	280.	282.	284.	286.	288.	290.	292.	294.

Figure 19. Mass Distribution from Geoid Residuals Relative to GEM-6

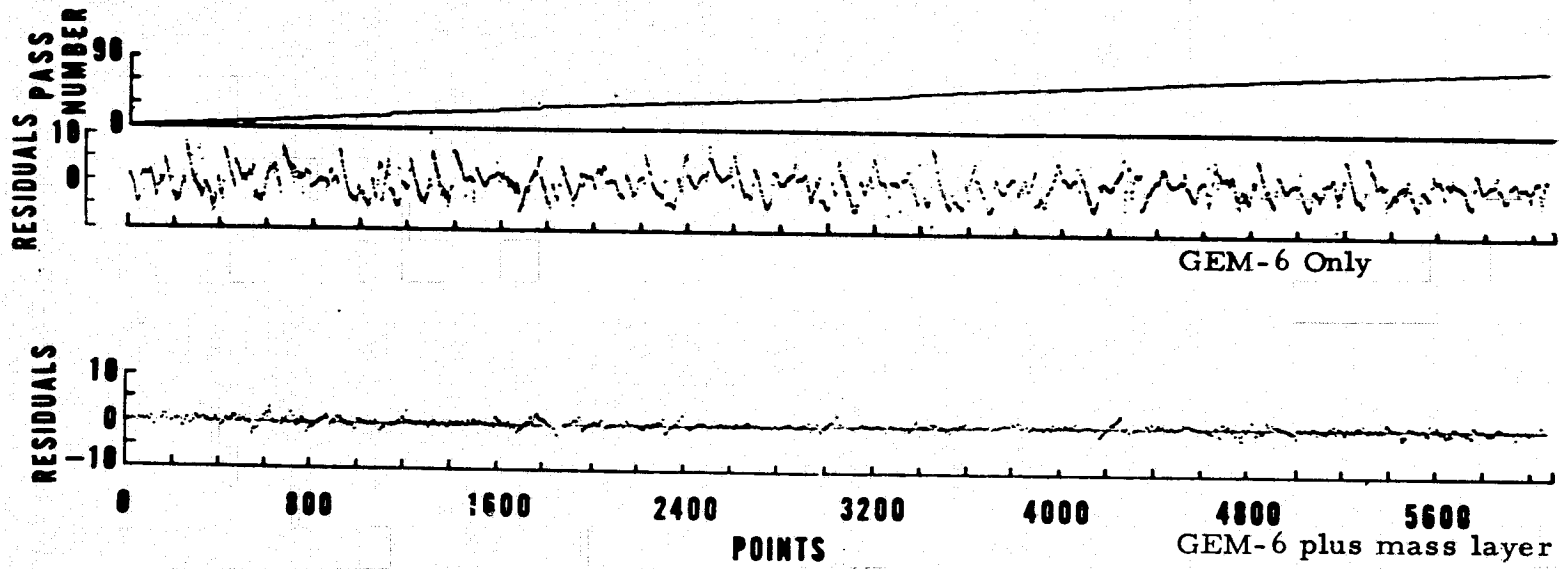


Figure 20. Geoid Residuals for GEM-6 and GEM-6 Plus Mass Layer

Solutions were also obtained for a mass layer at a depth of -111 km and for cases using a kernel with low degree harmonics removed. The primary effect of doubling the depth is an increase in RMS mass by a factor of 4 as one might expect. The much larger fluctuations indicate that the correlation between neighboring masses becomes excessive at -111 km. The fit of residuals decreased only about 2 percent when the depth was doubled. A truncated kernel caused significant mass changes mainly near the edges and hence a shift in the mean. RMS residuals remain essentially unaltered.

The contours of Figure 18a are mostly gentle. A negative region with trough of -5 m exists at about 33N, 285E. Highs of 10 meters can be seen at +27.5°N, 292°E and along the southern border. Some of these are probably due to edge effects. The total geoid in Figure 18b is the sum of GEM-6 and the mass layer contribution from Figure 18a. The composite model represents the smoothed observations to an RMS level of .71 m.

### 3.8 Gravity Anomaly Differences

The Defense Mapping Agency provided a total of 67 1° x 1° anomalies in the region 18° to 40° north latitude and 275° to 295° longitude. Unfortunately, only 11 of them were interior to our quad and, of these, most were near the edges where the accuracy is degraded (see Figure 9). Also, the average standard error of the observations was 13.6 mgal. The mean and RMS difference of the 11 interior anomalies with respect to the combined model was approximately +20 mgal independent of whether the mass layer was at a depth of -55.5 or -111 km\*. Even though there were some rather large residual changes for individual points, the mean and RMS did not depend on whether the computed values were point anomalies or anomalies averaged over the corners of the square. Nor do they depend on whether the full or truncated kernel propagated the mass layer. The mean difference decreased 2.5 mgal to 17.5 mgal when the calibration bias was removed\* and the RMS decrease was somewhat smaller at 2.2 mgal. The remaining bias discrepancy cannot be readily explained at this time. The gravity sample is really too small and the observation uncertainties too large. It should be mentioned that in all of the cases, the RMS difference about the mean was only 7 milligals.

---

\*These results can be shown analytically.

Table 8. Gravity Anomaly Differences

$\phi$	$\lambda$	$\hat{g}$	$g_e$	$\hat{g}_h$	$g_h$	$dg$	$\bar{g}_h$	$d\bar{g}$
34.5	285.5	-49.0	-27.3	-21.7	-26.3	4.6	-41.6	19.9
32.5	281.5	-5.0	-19.0	14.0	-8.8	22.8	7.5	6.5
31.5	283.5	-40.0	-25.9	-14.1	-42.8	28.7	-25.7	11.6
31.5	290.5	-35.0	-44.8	9.8	3.5	6.4	-4.8	14.6
31.5	291.5	-26.0	-46.3	20.3	-2.4	22.6	-2.3	22.5
30.5	291.5	-38.0	-48.5	10.5	-.5	11.0	1.8	8.6
29.5	290.5	-38.0	-48.7	10.7	-9.6	20.3	-3.1	13.7
29.5	291.5	-31.0	-50.3	19.3	19.0	.3	3.3	15.9
27.5	289.5	-30.0	-48.9	18.9	-5.7	24.6	-9.6	28.5
25.5	287.5	-17.0	-44.4	27.4	4.1	23.3	8.8	18.6
25.5	289.5	-37.0	-49.9	12.9	-11.1	24.0	-3.7	16.6

Table 8 shows the results from an example run with the mass layer at -55.5 km,  $C_{40}^* = -.254 \times 10^{-6}$  and bias removed. The definitions of the symbols are:

$\phi, \lambda$  = Latitude, longitude, respectively (degrees)

$\hat{g}$  = Observed  $1^\circ \times 1^\circ$  anomaly from DMA - milligals

$g_e$  = GEM-6 anomaly

$\hat{g}_h = \hat{g} - g_e$  = "observed" high degree anomaly

$g_h$  = Computed gravity from mass layer

$dg = \hat{g}_h - g_h$

$\bar{g}_h$  = Computed gravity averaged over center and corners of  $1^\circ \times 1^\circ$  square

$d\bar{g} = \hat{g}_h - \bar{g}_h$

The large differences between  $g_h$  and  $\bar{g}_h$  suggest that the gravity field due to the layer is too rough and that the finite shape masses should do better. We could weight the gravity data in the mass layer regression but the sample size seems too small at present to have much difference. Further investigations are needed to resolve the differences. Unfortunately, time and funding did not permit continuation of the current effort.

### 3.9 Conclusions and Remarks

- o The crossing differences provide an excellent measure of consistency on the altimetry and ephemeris. With moderate care in editing, RMS crossing differences (after adjustment) of less than 0.9 meters are attainable. The RMS bias corrections indicate an ephemeris precision on the order of 2.3 meters.
- o Relative to an ellipsoid of flattening =  $1/298.255$ , the mean and RMS geoid residual with respect to GEM-6 over the Atlantic area examined were 0.86 m and 3.45 meters, respectively (after application of the calibration bias). The mean residual corresponding to the actual value of  $C_{40}$  in GEM-6 is 5.1 meters.
- o A grid of mass points with 1 degree spacing at 55.5 km beneath the surface fits the residual geoid signature to a level of 0.71 meters RMS. Using minimum variance weighting, the formal error estimate for a mass near the center of the distribution is about  $0.3 \times 10^{-9}$  earth mass.
- o Thus far, comparisons between observed and inferred gravity have been inconclusive due to small sampling, marginal surface data quality, and apparent roughness of the mass layer. Further investigations are needed to resolve the bias of some 17.5 milligals for the 11 points over the area.



## APPENDIX 1

### COMPARISON OF DISK AND POINT MASS POTENTIALS AT DEPTH

Two cases are of interest. The first is one where both disk and point are placed at the same depth with masses such that they produce the same potential or geoid height shift at the intersection of the disk axis and the earth's surface. Let the depth of both masses be  $Z = nb$  where  $b$  is the disk radius and  $Z$  is distance along the disk axis from the center. The mass of the point source required to produce a height  $N_{po}$  is given by:

$$\frac{m}{M} = \frac{nb}{a} N_{po} \quad (1)$$

$M$  is the earth's mass and  $a$  the mean earth radius. The height shift along the disk axis at distance  $\zeta = Z/b$   $N_{do}$

$$N_{do} = \frac{2\pi\sigma ba^2}{M} (\sqrt{1+\zeta^2} - \zeta) \quad (2)$$

where  $\sigma$  is the density (mass/area). Hence,

$$\frac{\sigma}{M} = \frac{N_{do}}{2\pi ba^2 (\sqrt{1+\zeta^2} - \zeta)} \quad (3)$$

At points  $r, Z$  where  $r$  is distance from the disk axis ( $G$  = gravitational constant):

$$N_p = \frac{Gm}{\sqrt{r^2 + Z^2}} \frac{a^2}{GM} = \frac{nN_{po}}{\sqrt{\rho^2 + \zeta^2}} \quad (4)$$

$$N_d = \frac{I(\rho, \zeta) N_{do}}{2\pi(\sqrt{1+\zeta^2} - \zeta)} \quad (5)$$

where  $\rho = r/b$ ,  $\zeta = Z/b$  and  $I(\rho, \zeta)$  is an integral given in Appendix 2. Upon setting  $N_{do} = N_{po} = 1$ ,  $\zeta = n$ , we obtain the geoid shifts of the two masses at the same depth. Fig. 4 shows the heights for a disk and the percent differences defined by

$$p = 100 \left( \frac{N_d - N_p}{N_d} \right)$$

for values of  $\zeta = 1, 2$ .

The second case of interest is one in which both disk and point source have the same mass but are placed at different depths such that both produce the same shift at the surface. From (1) and (4) with  $N_{po} = 1$  meter,  $r = 0$ , and  $m = \pi b^2$ , we obtain

$$N_p = \pi b^2 \frac{\sigma}{M} \frac{a^2}{Z} \quad (6)$$

Substitute  $\sigma/M$  from (3) and set  $N_p = N_{do} = 1$ , then solve for  $Z = Z_d$ , define  $d_p \triangleq Z_d/b$ :

$$d_p = \frac{1}{2(\sqrt{1+\zeta^2} - \zeta)} \quad (7)$$

The value of  $d_p$  from (7) is used in (4) for points off of the axis. A point mass at depth  $d_p$  causes the same geoid shift at the surface as a disk with equal total mass oriented with axis parallel to the surface normal and disk center at depth  $\zeta$ . The percent differences for case 2 are much smaller than the previous ones indicating that the deeper mass approximates the disk potential better.

Consider next the gravity disturbance,  $\delta_g$ , arising from the masses. At the same depth with masses given by (1) and (3),

$$\delta g_p = \frac{\delta g_p'}{\gamma} = \frac{\frac{Gm}{b^2(\rho^2 + \zeta^2)}}{\frac{GM}{a^2}} = \frac{n N_{po}}{b} \frac{1}{(\rho^2 + \zeta^2)} = \frac{n}{b} \frac{1}{\rho^2 + \zeta^2}$$

where  $\delta g_p$  is in units of  $\gamma$ 's, and  $N_{po}$  is set equal to one meter. The disk acceleration is shown in Appendix 2 to be ( $l'$  also defined in Appendix 2):

$$\delta g_d = \frac{\delta g_d'}{\gamma} \frac{l'}{2\pi b(\sqrt{1+\zeta^2}-\zeta)}$$

This comparison of equal masses at different depths is obtained as before by holding  $\delta g_d$  fixed and calculating  $\delta g_p$  from a point mass located at  $\zeta = \zeta_d$ . The expression is simply:

$$\delta g_p = \frac{m}{M} \frac{a^2}{b^2} \frac{1}{(\rho^2 + \zeta^2)} = \frac{\zeta_d}{b(\rho^2 + \zeta^2)}$$

Note that in neither case does  $\delta g_p = \delta g_d$  at the surface. Since the masses and depths were chosen to give equal geoid height shifts, they cannot be made to have equal  $\delta g$ 's (i. e., derivatives) also.

## APPENDIX 2

### POTENTIAL AND ATTRACTION FROM A DISK

The potential of a thin disk having uniform density,  $\sigma$ , and radius,  $b$ , is given by (see Fig. 2-1 for the coordinates):

$$V = G\sigma \int_0^2 \int_0^b \frac{\bar{r} d\bar{r} d\theta}{S} ; \quad S = [Z^2 + \bar{r}^2 + r^2 - 2r\bar{r} \cos \theta]^{1/2}$$

Using normalized variables  $\rho = r/b$ ,  $\zeta = Z/b$ , and integrating with respect to  $\bar{r}$ , with the definitions:

$$g = \rho \cos \theta$$

$$f_1 = (1 - 2g + \rho^2 + \zeta^2)^{1/2}$$

$$f_2 = (\rho^2 + \zeta^2)^{1/2}$$

One finds,

$$\frac{V}{G\sigma b} = I_1 + \int_0^{2\pi} \left[ f_1 - f_2 + g \ln \left( \frac{1 - g + f_1}{f_2 - g} \right) \right] d\theta \quad (2.1)$$

$V = V(\rho, \zeta)$  were obtained by setting  $\zeta$  at constant depth and numerically integrating (2.1).

To find the attraction,  $\delta g$ , we note that:

$$\frac{1}{G\sigma} \delta g = \frac{1}{G\sigma b} \frac{\partial V}{\partial \zeta} = I_2 = \zeta \int_0^{2\pi} \left[ \frac{1}{f_2 - g} - \frac{1 + f_1}{f_1(1 - g + f_1)} \right] d\theta \quad (2.2)$$

When  $\rho = 0$ , both are simply integrable, and reduces to:

$$g = 0, \quad f_1 = \sqrt{1 + \zeta^2}, \quad f_2 = \zeta$$

$$V = 2\pi G\sigma b (\sqrt{1 + \zeta^2} - \zeta)$$

$$\delta g = 2\pi G\sigma \left(1 - \frac{\zeta}{\sqrt{1 + \zeta^2}}\right)$$

which are the elementary expressions for the potential and attraction of a disk along the axis.

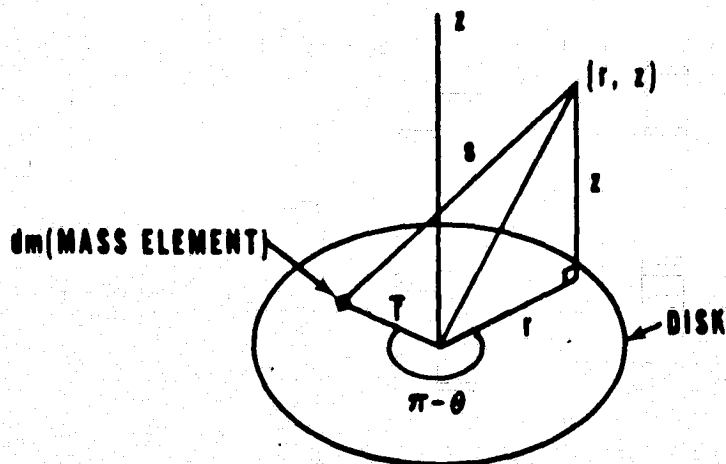


Figure 2-1. Disk Geometry

### Appendix III. Error Analysis of Truncated Kernels

Let the total potential at each field point,  $T$ , be represented by a surface integral over  $\sigma$ :

$$T = \int_{\sigma} \frac{dm}{\rho} = \int_1 \frac{dm}{\rho} + \int_2 \frac{dm}{\rho} \quad (3.1)$$

where region 1 is the part of  $\sigma$  with measurements and region 2 is the part without. Decomposing into low and high degree components designated by subscripts  $l$  and  $h$ , respectively, and using  $K$  for  $1/\rho$ , the actual high degree part of  $T$  is given by

$$T_h = T - T_l = \int_{1+2} K dm_h = \int_{1+2} (K_h + K_l) dm_h = \int_{1+2} K_h dm_h \quad (3.2)$$

The last equality invokes the orthogonality of  $K_l$  and  $dm_h$ . Consider the error incurred from using the kernels  $K$  and  $K_h$  over the region 1 integration. For the kernel  $K_h$ , the error is

$$\int_{1+2} K_h dm_h - \int_1 K_h dm_h = \int_2 K_h dm_h \quad (3.3)$$

Had one used  $K = K_l + K_h$ , the error would be

$$\begin{aligned} \int_{1+2} K_h dm_h - \int_1 (K_l + K_h) dm_h &= \int_2 K_h dm_h - \int_1 K_l dm_h \\ &= \int_2 K_h dm_h + \int_2 K_l dm_h = \int_2 K dm_h \end{aligned} \quad (3.4)$$

Use of the high degree kernel reduces the error by the amount  $\int_1 K_l dm_h$

$$= - \int_2 K_l dm_h.$$

From equations 3.3 and 3.4, the variance of  $T_h$  due to the truncation are

$$\sum_a = K_h \sum_h K'_h, \quad \sum_b = K \sum_h K' \quad \text{respectively,}$$

and since  $|K| > |K_h|$  we can expect a smaller error from use of the high degree kernel. In practice,  $K_h$  is simply given by

$$K_h = \frac{a}{\rho} - \sum_{n=0}^{\ell} P_n(\cos \psi)$$

where  $\ell$  is the degree of removal.

## References

- [1] P. Muller, W. Sjogren, Mascons: Lunar Mass Concentrations, Science, Vol. 161, No. 3842, August 1968.
- [2] W. L. Sjogren, P. Gottlieb, P. Muller, W. Wallenhaupt, Lunar Gravity Via Apollo 14 Doppler Radio Tracking, Science, Vol. 175, p. 165, 1972.
- [3] W. Sjogren, P. A. Laing, A. S. Lui, R. Wimberly, GEOS-3 Experiment Final Report: Analysis of SST Doppler Data for the Determination of Earth Gravity Field Variations, JPL Report, May 1976.
- [4] B. Tapley, D. Ingram, Lunar Orbit Determination in the Presence of Unmodeled Accelerations, AAS/AIAA Astrodynamics Conference, Paper 71-37, August 1971.
- [5] D. S. Ingram, Orbit Determination in the Presence of Unmodeled Accelerations, AMRL Report No. 1022, University of Texas, January 1971.
- [6] L. Wong, G. Buechler, W. Downs, W. Sjogren, P. Muller, P. Gottlieb, A Surface Layer Representation of the Lunar Gravitational Field, JGR, Vol. 76, No. 26, September 10, 1971.
- [7] W. Sjogren, J. Lorell, L. Wong, W. Downs, Mars Gravity Field Based on a Short Arc Technique, JGR, Vol. 80, No. 20, July 10, 1975.
- [8] D. C. Fraser, A New Technique for the Optimal Smoothing of Data, PhD Thesis T474, MIT, January 31, 1967.
- [9] D. E. Smith, etc., Contributions to the National Geodetic Satellite Program by GSFC, JGR, Vol. 81, No. 5, February 10, 1976.



- [10] C. L. Ayers, Synthesized and Transmission Frequencies for ATS-F Tracking, informal document and handwritten notes, 1974.  
J. R. DeMeo, ATSR, DRS, Mode Data Utilization Algorithms, GSFC Memorandum, 1974.
- [11] C. F. Martin, M. L. Butler, Calibration Results for GEOS-3 Altimeter, NASA CR-141430, September 1977.
- [12] M. S. Molodenski, etc. Methods for Study of the External Gravitational Field and Figure of the Earth, Translation by Israel Prog. for Sci Translations, 1962.
- [13] B. Chovitz, Determination of Density of a Simple Layer Directly from Geoid Height, JGR, Vol. 79, No. 20, July 10, 1974.
- [14] W. A. Heiskanen, H. Moritz, Physical Geodesy, Freeman & Co., 1967.
- [15] J. Junkins, An Investigation of Finite Element Representation of the Geopotential, AAS/AIAA Paper 75-078, July 1975.
- [16] R. Rapp, Methods for the Computation of Detailed Geoids and Their Accuracy, Ohio State University, Department of Geodetic Science, Report No. 233, November 1975.

1. Report No. NASA CR-141438	2. Government Accession No.	3. Recipient's Catalog No.	
4. Title and Subtitle Analysis of Satellite-to-Satellite Tracking (SST) and Altimetry Data from GEOS-C		5. Report Date April 1978	
		6. Performing Organization Code	
7. Author(s) L. Wong, E. Matthews, and W. Downs		8. Performing Organization Report No.	
9. Performing Organization Name and Address The Aerospace Corporation Development Operations El Segundo, CA 90245		10. Work Unit No.	
		11. Contract or Grant No. NAS6-2508	
12. Sponsoring Agency Name and Address National Aeronautics and Space Administration Wallops Flight Center Wallops Island, VA 23337		13. Type of Report and Period Covered Contractor Report	
		14. Sponsoring Agency Code	
15. Supplementary Notes			
16. Abstract  <p>The objective of this study is to infer the exterior gravitational field of the earth and the structure of the geoid from GEOS-C metric data. Of the many measurement types available, the scope of our effort is limited to two: satellite-to-satellite range and range rate tracking (SST) and radar altimetry. This analysis effort separated naturally into two parts: inference of the long wavelength disturbances from SST and the fine structure geoid from altimetry.</p> <p>Under the SST analysis, a direct point-by-point estimate of gravity disturbances by means of a recursive filter with backward smoothing was initially attempted but had to be forsaken due to poor convergence (attributed to inadequate signal-to-noise ratio). The adopted representation consists of a more or less uniform grid of discrete masses at a depth of approximately 400 km from the earth's surface. The layer is superimposed on a spherical harmonics model.</p> <p>Under altimetry, the procedure for smoothing the altimetry and inferring the fine-structured gravity field over the Atlantic test area is described. We again chose to represent the local disturbances by means of a density layer. The altimeter height biases were first estimated by a least squares adjustment at orbital crossover points. After taking out the bias, long wavelength contributions from GEM-6 as well as a calibration correction were subtracted. The residual heights were then represented by a mass distribution beneath the earth's surface.</p>			
17. Key Words (Suggested by Author(s))  GEOS-3 altimetry satellite-to-satellite tracking geoid		18. Distribution Statement  Unclassified - unlimited STAR Category - 13,17,42	
19. Security Classif. (of this report) Unclassified	20. Security Classif. (of this page) Unclassified	21. No. of Pages 75	22. Price*